International Journal of Engineering Science 166 (2021) 103515

Contents lists available at ScienceDirect

International Journal of Engineering Science

journal homepage: www.elsevier.com/locate/ijengsci

Importance of microstructure modeling for additively manufactured metal post-process simulations

Sumair Sunny, Glenn Gleason, Karl Bailey, Ritin Mathews, Arif Malik*

Department of Mechanical Engineering, The University of Texas at Dallas, Richardson, TX 75080, USA

ARTICLE INFO

Article history:
Received 11 February 2021
Revised 7 May 2021
Accepted 6 June 2021

Keywords:
Microstructure modeling
Finite element analysis
Metal additive manufacturing
Micro-milling
Laser shock peening
Anisotropic material response

ABSTRACT

This work investigates the significance of microstructure-level modeling by simulating the material response of an inhomogeneous selective laser melted (SLM) Inconel 625 specimen subjected to two different post-process operations, namely micro-milling and laser shock peening (LSP). A physics-based thermal finite element simulation is executed to obtain the SLM thermal history from which a 3-dimensional inhomogeneous microstructure representative volume element (RVE) is generated via the Dynamic Kinetic Monte Carlo predictive model. A Johnson–Cook plasticity definition coupled with Hall–Petch strengthening is used to define unique yield surfaces for individual grains based on their major diameters. Micro-milling and LSP simulations are subsequently executed with and without considering an inhomogeneous microstructure RVE in attempt to elucidate differences in the plastic strain, temperature, induced stress magnitude and distribution, as well as differences that arise during material removal for the micro-milling only. The micro-milling simulations reveal a greater volumetric distribution of plastic strain and temperature for the inhomogeneous case, although the homogeneous case with isotropic assumption reveals greater heat dissipation at the tool-workpiece interface with 27% greater contact pressure and 39% greater frictional shear stress. Examining the ductile and shear damage progression at a specific time increment reveals that the inhomogeneous model has a slightly lower damage propensity in comparison the homogeneous case, despite having identical damage models and boundary conditions. Variation in the SLM process-dependent yield surfaces, for grains at different locations, results in spatial variations of the computed stress triaxiality, which influences the material removal, as well as the stress concentrations developed near the tool-workpiece interface. Thus, a process-structure-property relationship is captured with the microstructure modeling. This work is the first to illuminate the importance of capturing SLM-induced anisotropy, considering the additively manufactured grain structure subject to micro-milling and LSP post-processes.

1. Introduction

The understanding of microstructure-specific material response, such as distribution of residual stress (RS) in a manufactured component for example, is an important factor towards determining the mechanical performance it can deliver. While experimental, analytical, and numerical methods exist to characterize RS, their results and usefulness can vary significantly

---

* Corresponding author.
E-mail address: Arif.Malik@utdallas.edu (A. Malik).

https://doi.org/10.1016/j.ijengsci.2021.103515

depending on (1) the degree of volumetric “averaging” in experimentally measured RS, and (2) the accuracy of material constitutive behavior representation in analytical and numerical models. A rigorous consideration of microstructure in predictive models may provide for better estimation of the state of stress during and after metal post-process operations. In this work, the influence of an *inhomogeneous* microstructure, induced by selective laser melting (SLM) type additive manufacturing, is investigated in conjunction with micro-milling and laser shock peening (LSP) post processes. These processes are studied considering that their respective strain rates differ by approximately two orders of magnitude, 10^4 and 10^6 s^{-1}, respectively (Wu & Zhang, 2014; Zhou et al., 2013). To distinguish the technical approach and findings of the demonstrated work, prior experimental, analytical and numerical attempts to characterize the microstructure-specific material response induced by micro-milling and laser shock peening are first discussed.

Various numerical techniques to model microstructure-specific response can be found in literature. Typically, microstructure modeling in finite element methods is achieved by either heterogeneous representative volume element (RVE) replication of the different phases (Chuzhoy, DeVor, Kapoor, & Bammann, 2002; Ljustina, Larsson, & Fagerström, 2014), or inhomogeneous RVE replicating the individual grains based on morphology, as well as porosity and other defects (Chen, Wang, Kysar, & Yao, 2007; Sunny, Gleason, Mathews, & Malik, 2021; Wang, Kysar, & Yao, 2008). Capturing the microstructure-specific response in orthogonal cutting/turning models has been found to offer improved insight towards the distribution of RS in the machined component, whilst also providing better prediction of cutting forces and chip morphology, as summarized in Table 1. Capturing the microstructure-specific response in laser shock peening (LSP) models has revealed anisotropic material response with asymmetry in the RS distribution, as summarized in Table 2.

Contrary to the studies discussed in Table 2, researchers whose focus was not influenced by microstructure resorted to FE models for LSP that assumed material isotropy and homogeneity. They obtained RS distributions exhibiting perfect symmetry and axisymmetry (Brockman et al., 2012; Correa et al., 2015; Warren, Guo, & Chen, 2008). Simulations by Warren et al. revealed significant difference when compared with X-ray diffraction (XRD) measurements of surface RS (Warren et al., 2008). Disregarding the plausible anisotropic response from the material considering the underlying microstructure, they attributed the discrepancy to: (1) averaging of the RS in the XRD technique, (2) inability to locate the exact LSP shot center for XRD measurement, and (3) numerical errors. In addition, Brockman et al. stated that XRD measurements could be misleading as the resolution may not necessarily allow complete details of the RS field to be captured (Brockman et al., 2012).

The importance of microstructure consideration in numerical models, especially in cases involving inhomogeneity and/or heterogeneity is evident from the literature, however, none of the models considered microstructure arising from an SLM build. Milling simulations in the literature do not highlight the importance of the ductile and shear damage parameters, nor do they discuss how these damage parameters are influenced during the cut. XRD measurements with limited spatial resolution, are subject to averaging, and hence cannot comprehensively capture the nuances in RS distribution. In addition, it should be noted that the studies in Tables 1 and 2 that do feature microstructure modeling (although not from SLM) relied on optical micrographs or EBSD images, and thus were based on 2D representations of the grain structure. While a 2D approach may sufficiently capture the in-plane material response at lower computational cost, assumptions have to be made regarding the out-of-plane behavior. Hence, a need for 3D predictive modeling of the SLM microstructure and its influence on post-processing operations, such as micro-milling or LSP, is recognized.

This work therefore seeks to elucidate the degree to which 3D microstructure consideration in finite element models influences the post-process material response. To achieve this, an *inhomogeneous* microstructure, produced by SLM, is subjected to micro-milling and LSP simulations. In the case of micro-milling, the influences of microstructure modeling on volumetric plastic strain, temperature distributions, induced stress, and material removal (considering the effects of ductile and shear damage parameters) are examined, while for LSP, the influences of microstructure modeling on the RS magnitude and distribution are examined. Accordingly, Section 2 describes an experimentally calibrated, physics-based thermal FE simulation from which the SLM thermal history is obtained. The thermal history is then used for 3D prediction and reconstruction of a Monte Carlo-based (Johnson et al., 2018; Rodgers, Bishop, & Madison, 2018) inhomogeneous microstructure RVE. Micro-milling and LSP simulations that are executed both with and without the RVE to capture inhomogeneous and anisotropic behavior are subsequently discussed in Section 2 and 3, along with a description of the material plasticity model and damage criteria. Trends in plastic strain, temperature, residual stress and material removal from simulations with and without microstructure are presented in Section 5. Finally, insights from both simulations highlighting the importance of microstructure modeling are summarized in Section 6.

2. Numerical approach

In this work, the microstructure of a cube-shaped Inconel 625 workpiece having a 1 mm edge length is predicted. In contrast to fabrication processes such as casting and forging, which form highly equiaxed grain structures (Trosch, Strößner, Völkl, & Glatzel, 2016), EBSD imaging for SLM parts has revealed the presence of elongated (columnar) and equiaxed (spherical) grains (Antonysamy, Meyer, & Prangnell, 2013). Since the microstructure of SLM parts is greatly influenced by rapid thermal cycles in the AM process, FE modeling to obtain the transient thermal history is an important aspect, and is discussed next. It should be noted that RS fields induced by the SLM process can be obtained using a thermomechanical analysis rather than just the thermal analysis, with the RS subsequently mapped over reconstructed grains in the post-process FE model. However, since one of the aims in the demonstrated work is to highlight the difference in RS patterns that arise during the post-process operation with inclusion of microstructure modeling, the SLM induced RS fields are omitted.

Table 1
Summary of investigations examining microstructure-specific material response induced by orthogonal cutting and turning.

Author (Year)	Approach; Material	Summary of key findings, details and modeling simplifications relevant to the present work
Chuzhoy et al. (2002)	Finite element (FE) modeling, Experimental; Ductile cast iron	• Introduced the concept of microstructure-level modeling, demonstrating its efficacy by simulating a 2D orthogonal cutting process for a ductile cast iron specimen having a heterogeneous microstructure of graphite nodules with ferrite and pearlite grains. A representative volume element (RVE) was used to discretize the microstructure within the finite element (FE) mesh, based on a photomicrograph of the material. Although not demonstrated, they mentioned that the 'random nature' of grain size and distribution could be captured using the Monte Carlo method. • Used an internal state variable model (Bammann, Chiesa, Johnson et al., 1996) to capture the behavior of each phase within the material, which was dependent upon strain, strain rate, temperature and amount of damage. Strain rate and temperature dependency had to be characterized experimentally for both ferrite and pearlite. • The predicted in-plane stress, strain, temperature and damage was reported to have good correlation with experiment observations in the literature. • Unlike 'traditional' FE models for machining, microstructure-level modeling elucidated new insights including how deformation would occur along grain boundaries, how grains could either be elongated/stretched or squeezed depending on their position relative to the tool, and most importantly, how damage would propagate through the heterogeneous structure.
Ljustina et al. (2014)	Finite element (FE) modeling, Experimental; Cast iron	• Performed a similar 2D FE study to that of Chuzhoy et al. (2002), with the emphasis on chip formation during orthogonal cutting of cast iron. • Heterogeneous microstructure observed in optical micrographs was mapped into the 2D FE mesh, capturing the different phases (graphite, ferrite, pearlite). • A Johnson–Cook (J-C) plasticity model was used in conjunction with a J-C ductile damage criterion. • Predicted and experimentally observed chip morphology showed good agreement.
Pan, Shih, Garmestani, & Liang (2019b)	Analytical, Experimental; Ti-6Al-4V	• Proposed a hybrid analytical method that accounted for thermal and mechanical effects, as well as dynamic recrystallization while predicting RS during the orthogonal turning of Ti-6Al-4V. • A Johnson-Mehl-Avrami-Kolmogorov (JMAK) model, which assumed random distribution of nucleation sites, was used to compute evolution in grain size taking into account thermal effects of the turning process, while a *modified* J-C model computed the flow stress evolution as a result of grain growth-induced thermal softening. • Average grain size was quantified by electron backscatter diffraction (EBSD) imaging of the microstructure, and the Hall–Petch (H-P) relation was subsequently used to compute initial yield stress, which was then coupled into the J-C equation. Next, a hybrid McDowell algorithm was used for RS calculation. • The predicted RS in the cutting and transverse directions showed reasonable agreement with X-ray diffraction (XRD) measurements, albeit differences were observed at shallow depths from the surface of the cut. An earlier study by Pan, Feng, Ji, & Liang (2018) demonstrated similar results when predicting the RS induced by turning of AISI 4130 steel.
Lu, Pan, Bocchini, Garmestani, & Liang (2019)	Analytical, Experimental; Ti-6Al-4V	• Compared a grain-size sensitive mechanical threshold stress (MTS) model (MacDougall & Maudlin, 2000) to a J-C model integrated with the H-P relation during the orthogonal cutting of Ti-6Al-4V. • The *modified* MTS model allows for instantaneous grain size calculation by considering the effects of dynamic recrystallization as the material was being machined, effectively capturing microstructural evolution. • A unique J-C plasticity definition was implemented for each of the respective alpha and beta phases of Ti-6Al-4V. The average grain diameter for each of the two phases was used to compute its respective yield stress, per H-P strengthening. The yield stresses obtained were then integrated into the J-C equation to compute respective flow stresses for each of the two phases. This approach is similar that described by Pan, Liang, & Garmestani (2019a). • Comparing the cutting and thrusting force components from both their modified MTS model and their J-C H-P model to experimental measurements from literature (Pan et al., 2019a), it was found that the modified MTS model would predict higher values of cutting force in comparison to the J-C H-P model, yielding better predictions at lower feed rates. The modified MTS model, however, predicted lower magnitudes of RS than what was experimentally documented in the literature (Ratchev, Afazov, Becker, & Liu, 2011).

Table 2
Summary of investigations that examine the microstructure-specific material response induced by laser shock peening.

Author (Year)	Approach; Material	Summary of key findings, details and modeling simplifications relevant to the present work
Chen et al. (2007)	Experimental characterization and 3D finite element (FE) modeling; Single crystal aluminum	• Investigated the anisotropic response induced by microscale LSP on single crystal aluminum, considering that the beam spot size is of the same order as grain size, therefore material properties were treated as anisotropic and inhomogeneous rather than assuming isotropy and homogeneity. Note, a single shot was applied at each peening location. • Spatial distribution of RS was measured by X-ray microdiffraction, along different crystalline directions on the treated surface, while atomic force microscopy (AFM) was used to measure plastic deformation on the treated surface. • Electron backscatter diffraction (EBSD) was used to measure crystal lattice rotation due to plastic deformation. • A 3D single crystal plasticity finite element analysis was employed to study the influence of crystal orientation, and revealed similar trends to those observed experimentally. • While an axisymmetric Gaussian pressure distribution was applied in the simulation, the predicted lattice rotation about the shock center was not axisymmetric due to the anisotropic characteristic of the single crystal. • Stress contour plots obtained via X-ray microdiffraction revealed a lack of symmetry in the RS distribution. • The study introduced a method to simulate anisotropic plastic behavior by capturing finite lattice rotations, however, the authors noted that future work would need to account for the influence of strain rate dependency, hardening and dynamic loading.
Wang et al. (2008)	Analytical, experimental and numerical; Single crystal aluminum	• This study was a follow-up to the investigation by Chen et al. (2007), wherein the LSP spot size was on the same order of magnitude as the grain size, therefore material properties were treated as anisotropic and inhomogeneous. • Anisotropic slip line theory was employed to derive stress and deformation fields induced via micro-LSP on single crystal aluminum, oriented such that plane strain conditions could be assumed. • Electron backscatter diffraction (EBSD) was used to measure crystal lattice rotation due to plastic deformation. • Good agreement was found when comparing the size of the predicted deformed region to that measured via AFM. • FE model results revealed asymmetric RS and distortion patterns despite the Gaussian pressure distribution. In addition, they revealed similar trends in lattice rotation distribution to that observed via EBSD measurements. • The study elucidated the importance of considering material properties to be anisotropic, however, the authors noted that rate and inertial effects as well as a more accurate temporal and spatial evolution of the plasma pressure distribution would need to be investigated in future work.
Cuellar, Hill, DeWald, & Rankin (2012)	Experimental and FE modeling; Ti-6Al-4V	• Investigated the effect of different LSP patterns on RS distribution and fatigue performance on a Ti-6Al-4V specimens featuring a hole. The underlying rationale was that geometric features such as notches and holes act as typical fatigue crack initiation points. Symmetric and axisymmetric LSP treatments were applied around the axis of the hole, in order to induce compressive RS, thereby improving fatigue life of the part. • Specimens used in the experiments were fabricated from *beta-solution-treated and over-aged* (BSTOA) Ti-6Al-4V having extra-low interstitials. The BSTOA heat treatment was reported to provide a transformed beta microstructure, having large and variable grains with sizes on the order of 1 to 2 mm. • Observations of the as-machined, heat treated specimen revealed a symmetric stress distribution on either side of the hole prior to LSP treatment. Observations made post-LSP treatment, using the contour method (Schajer, 2013) to create a 2D map of RS induced on either side of the hole, revealed an asymmetric, non-uniform RS distribution. Considering the symmetric and axisymmetric LSP treatment pattern around the hole, it is plausible that the asymmetric RS distribution resulted from either the inhomogeneous microstructure or the LSP shot sequence.
Rozmus-Górnikowska, Kusiński, & Cieniek, 2020	Experimental; Inconel 625	• Assessed the influence of LSP treatment on surface topography, microstructural changes, surface roughness and surface hardness of wrought, solid-solution-strengthened Inconel 625. • Scanning electron microscopy imaging revealed a high density of slip bands on the treated surface and along the cross section of the treated specimen. The presence of slip bands was also confirmed via AFM. • Cracking of carbide precipitates, formed on the extension of slip bands, was observed on the surface and through the cross section of the specimen. The authors also suggest that the large plastic deformation induced could cause cracking of carbides, but the phenomena is also indicative of high localized compressive stress. • High strain-rate conditions, characteristic to LSP, were noted to be conducive to slip band formation. This was supported by transmission electron microscopy images that revealed dense, near-surface slip bands. • AFM revealed that the average roughness increased from 100 nm to 1 μm, while nanohardness tests revealed an increase in surface hardness from approximately 270 HV to 350 HV. The increase in hardness was attributed to high density of near-surface dislocations and slip bands produced by LSP treatment. • The work demonstrated the influence of LSP on microstructure, however, it did not discuss the extent to which the existing microstructure could influence the findings. Similar findings have also been reported by Chen, Sun, Li, & Ren (2020a), who examined how a combination of heat treatment and LSP can alter the microstructure and mechanical properties of SLM Inconel 625 parts.

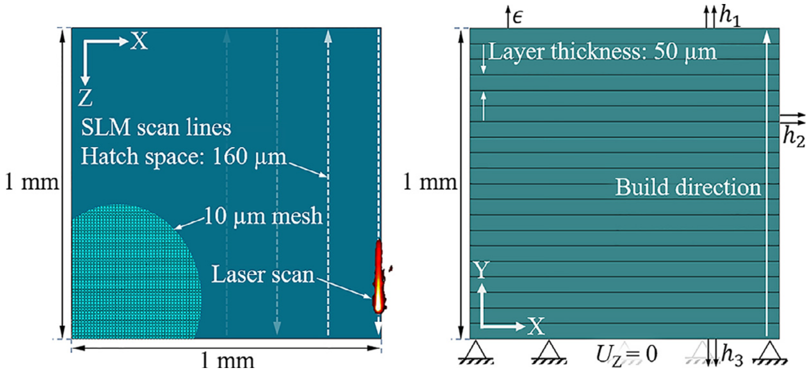

Fig. 1. Schematic of the SLM FE model. (*Left*) Top view illustrating the scan lines and mesh resolution, (*Right*) Side view illustrating the deposited layer thickness, build direction and thermal and mechanical boundary conditions.

Table 3
Selective laser melting parameters (Wang et al., 2016a).

Parameters	Power, P	Scan speed, v	Scan pattern	Hatch spacing	Layer thickness
Values	360 W	0.4 m s^{-1}	Bi-directional	160 μm	50 μm

2.1. Thermal finite element selective laser melting simulation

An experimentally calibrated, physics-based thermal FE simulation is used to obtain the SLM thermal history from which the dimensions of the melt pool and heat affected zone are extracted. These dimensions are then iteratively imported into the Dynamic Kinetic Monte Carlo microstructure prediction model (Sunny, Yu, Mathews, Malik, & Li, 2021a) by which the 3D inhomogeneous microstructure RVE is determined.

The powder continua that is scanned to build the AM cube is modeled with a structured cubic mesh featuring elements of 10 μm edge length, as illustrated in Fig. 1. A Python script is employed to control the sequential deposition of each 50 μm thick powder layer. The deposition process is implemented using the inactive elements approach (Denlinger & Michaleris, 2016; Lindgren, Lundbäck, Fisk, Pederson, & Andersson, 2016; Michaleris, 2014). Similar to the approach adopted by Madireddy, Li, Liu, & Sealy (2019), as a modeling simplification the substrate is replaced with a displacement boundary condition limiting motion in the vertical (Y) direction, and to compensate for the heat conduction through the surrounding powder (not modeled) as well as the substrate, artificial convective heat transfer coefficients (h_2 and h_3) are calibrated on the relevant surfaces. The simplification helps reduce computational expense.

The thermal FE simulation applies the SLM parameters listed in Table 3. Eqs. (1)–(4) govern the 3D spatial and temporal temperature field distribution for both the powder and fused (solid) continua during the SLM process. Note that similar metal AM modeling approaches have been adopted by Heigel, Michaleris, & Reutzel (2015); de La Batut, Fergani, Brotan, Bambach, & El Mansouri (2017); Manvatkar, Gokhale, Reddy, Venkataramana, & De (2011); Zhao, Iyer, Promoppatum, & Yao (2017).

$$\frac{\partial}{\partial x}\left(\mathrm{k}\frac{\partial T}{\partial x}\right)+\frac{\partial}{\partial y}\left(\mathrm{k}\frac{\partial T}{\partial y}\right)+\frac{\partial}{\partial z}\left(\mathrm{k}\frac{\partial T}{\partial z}\right)+\mathrm{Q}=c_p\rho\frac{\partial T}{\partial t},\quad \text{for } t\geq 0 \tag{1}$$

In Eq. (1), T is the temperature at time t, c_p is the specific heat, ρ is the material density, k is the thermal conductivity, and Q represents the volumetric heat flux (Denlinger, Gouge, Irwin, & Michaleris, 2017; Gouge & Michaleris, 2017) induced by the laser. Temperature-dependent properties vary for both the powder and solid continua (Daw, Rempe, & Knudson, 2010; Wang et al., 2017). Neglecting pre-heating effects, the initial temperature, t_0, for each powder layer L deposited over the last scanned layer is assigned as the ambient (sink) temperature T_∞ within the print environment (assumed to be 296 K), per Eq. (2).

$$T(t_{0,L})=T_\infty \tag{2}$$

Goldak et al.'s double ellipsoid Gaussian heat source model (Goldak, Chakravarti, & Bibby, 1984), defined by Eq. (3), is employed to describe the spatial and temporal heat flux distribution induced by the laser. The model, depicted in Fig. 2, is scripted in a Fortran user-subroutine (DFLUX) to control motion of the volumetric heat flux during the SLM simulation.

$$\mathrm{Q}=\begin{cases}\dfrac{6\sqrt{3}\mathrm{f_f}\mathrm{P}\Lambda}{\mathrm{abc_f}\pi\sqrt{\pi}}\mathrm{e}^{-3\frac{\mathrm{x}^2}{\mathrm{a}^2}}\ \mathrm{e}^{-3\frac{\mathrm{y}^2}{\mathrm{b}^2}}\ \mathrm{e}^{-3\frac{(\mathrm{z}+\mathrm{v}t)^2}{\mathrm{c_f}^2}}, & \forall\ \mathrm{z}\geq \mathrm{z_i}\ \ \text{for}\ \ \mathrm{t}>0\\ \dfrac{6\sqrt{3}\mathrm{f_r}\mathrm{P}\Lambda}{\mathrm{abc_r}\pi\sqrt{\pi}}\mathrm{e}^{-3\frac{\mathrm{x}^2}{\mathrm{a}^2}}\ \mathrm{e}^{-3\frac{\mathrm{y}^2}{\mathrm{b}^2}}\ \mathrm{e}^{-3\frac{(\mathrm{z}+\mathrm{v}t)^2}{\mathrm{c_r}^2}}, & \forall\ \mathrm{z}<\mathrm{z_i}\ \ \text{for}\ \ t>0\end{cases} \tag{3}$$

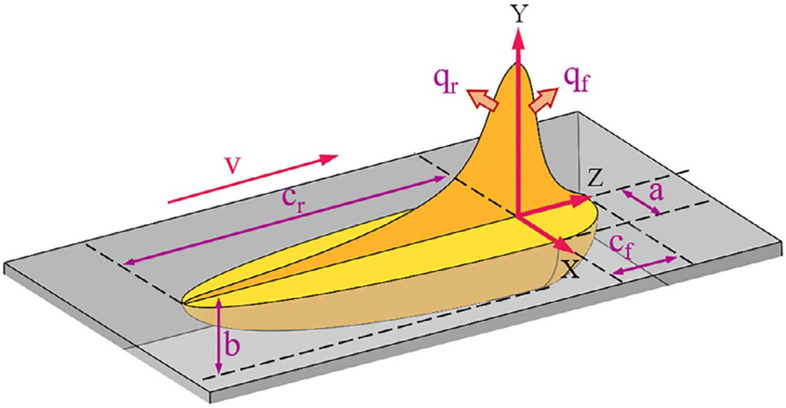

Fig. 2. Double ellipsoid heat source model (Goldak et al., 1984).

Table 4
Heat source model geometric parameters (Sunny, Yu, Mathews, Malik, & Li, 2021a).

Parameter	Values
a	160 μm
b	160 μm
c_f	276 μm
c_r	1520 μm
f_f	1.4
f_r	0.6

Table 5
Thermal parameters for SLM simulation using Inconel 625 (Sunny, Yu, Mathews, Malik, & Li, 2021a).

Thermal parameters	Λ	ϵ	h_1	h_2	h_3
Values	0.67	0.67	12 W m^{-2} K^{-1}	10 W m^{-2} K^{-1}	1000 W m^{-2} K^{-1}

In Eq. (3), P is the laser power input, Λ is the absorption efficiency of the powder particles, z_i is the instantaneous Lagrangian Z ordinate (assuming the scan proceeds in the z direction), and ratios f_f and f_r control respective heat flux portions q_f and q_r that are distributed amongst the front and rear quadrants of the heat source. Geometric parameters for Eq. (3), which are fitted to replicate the melt pool (MP) geometry trend for Inconel 625, as reported by Heigel & Lane, 2018, are given in Table 4.

Internal conduction as well as convection and radiation on free surfaces Γ of the active elements give rise to heat transfer within the powder and fused continua. The surface energy balance, described by Eq. (4), is recalculated at every time increment during the thermal simulation, (Hahn & Özisik, 2012).

$$\mathrm{k}\nabla T \cdot \hat{\mathrm{n}} = h_i(T - T_\infty) + \sigma_{SB}\epsilon\left(T^4 - {T_\infty}^4\right) \quad \text{on free surfaces } \Gamma \tag{4}$$

In Eq. (4), h_i are the convective heat transfer coefficients, σ_{SB} is the Stefan–Boltzmann constant (5.6703×10^{-8} W m^{-2} K^{-1}), ϵ denotes the emissivity, and $\hat{n}$ is the unit normal vector to free surfaces Γ. Thermal parameters for heat transfer in the SLM simulation, including Λ (which depends on mean particle size and distribution), are provided in Table 5. Solutions for the SLM process are computed using the implicit solver of Abaqus v6.14. Since only a thermal solution is required for the microstructure prediction using the Dynamic Kinetic Monte Carlo (KMC) algorithm (discussed in Section 2.3), linear hexahedral diffusive heat transfer elements having only temperature degree of freedom are used.

2.2. Verification of non-occurrence of keyholes and/or porosities considering the SLM parameters

Modeling of microstructural defects, such as keyholes and/or porosities (Shrestha, Starr, & Chou, 2018, 2019) that may arise depending on the specific SLM process parameters is an important consideration that can influence the distribution of RS in the workpiece during post-process operations. Fig. 3 features optical micrographs of the cross section of a single

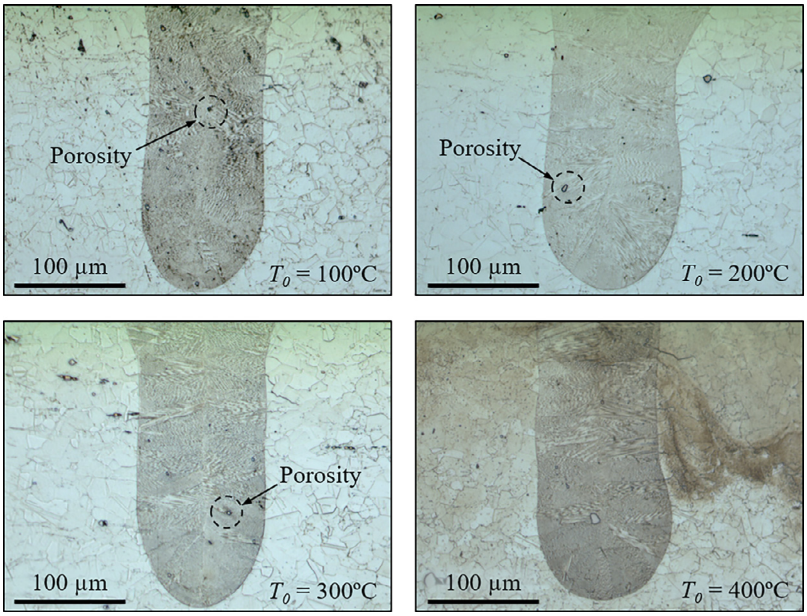

Fig. 3. Optical micrographs of the cross section of a single SLM scan track (plane perpendicular to scan direction) for Inconel 718, documented by Chen et al. (2020b). SLM process parameters: power: 350 W, scan speed: 0.5 m s^{-1}, substrate preheating temperature: (*Top Left*) 100 °C, (*Top Right*) 200 °C, (*Bottom Left*) 300 °C, (*Bottom Right*) 400 °C.

SLM scan track for Inconel 718, documented by Chen et al. (2020b), who examined the influence of preheating temperature on melt pool morphology. While their work encompassed numerous power and scan speed settings, the micrographs seen Fig. 3 represent a laser power of 350 W and a scan speed of 0.5 m s^{-1}, similar to that implemented in this work.

The thermophysical properties of Inconel 718 and 625 are quite similar (Parida & Maity, 2018; Zhong, Kittel, Gasser, & Schleifenbaum, 2019), making their "expected" tendency to exhibit pores comparable under the same set of process parameters. Contrary to expectation, Zhong et al. (2019) performed laser metal deposition experiments and found that Inconel 718 exhibits significantly greater porosity (0.69%) in comparison to Inconel 625 (0.009%) under identical experiment conditions. From Fig. 3, at the high-power setting of 350 W and a scan speed of 0.5 m s^{-1}, small spherical pores having approximate diameters of less than 5 μm are visible for low preheating temperatures (100 to 300 °C). At a preheating temperature of 400 °C, pores are no longer evident. Considering the size of the pores, relative to the size of the hexahedral cube-shaped elements in the FE simulation (10 μm edge length), as well as Zhong et al.'s findings, it is justified that porosity need not be considered in this work. It should be noted, however, that the quiet elements approach (Michaleris, 2014) can be readily adopted to accommodate porosities and keyhole defects if their sizes appear to be large enough to influence the RS distribution during post-process simulations.

2.3. *Reconstructing microstructure of the SLM workpiece in the post-processing FE models*

Once the transient thermal history is obtained, it is used to generate input for the Dynamic Kinetic Monte Carlo (KMC) microstructure prediction model (Sunny, Yu, Mathews, Malik, & Li, 2021a). It is worth noting that an alternative to the calibrated physics-based SLM thermal model is to use infrared (IR) thermographic imaging (Lane, Moylan, Whitenton, & Ma, 2016; Moylan, Whitenton, Lane, & Slotwinski, 2014) to provide data on temporal variations in the dimensions of the melt pool (MP) and heat affected zone (HAZ) for use by the Dynamic KMC microstructure model.

Following determination of the microstructure, individual grains G_i are reconstructed using Python scripting as a RVE in the Lagrangian FE model (Carlsson, 2013), as depicted in Fig. 4 (*Left*). A scripting routine is also implemented to assign unique material definitions, MAT_i, to the individual grains, G_i. These material definitions are based on the major diameter, d_i, of respective grains as seen in Fig. 4 (*Center*), since it is the major diameter of non-spherical grains that corresponds to the lowest strength direction in the polycrystalline alloy. It is this variation in material definitions among the grains which results in anisotropic plastic behavior, rather than crystalline orientations, which are not provided by the Dynamic KMC model. Yield strengths for each grain are calculated via Hall–Petch strengthening and the resulting maximum distortion energy criterion yield surfaces are depicted in Fig. 4 (*Right*), which illustrates the substantial variation in the quasi-static yield strengths for the inhomogeneous model. Material constitutive models for the micro-milling and LSP case studies are discussed in subsequent sections.

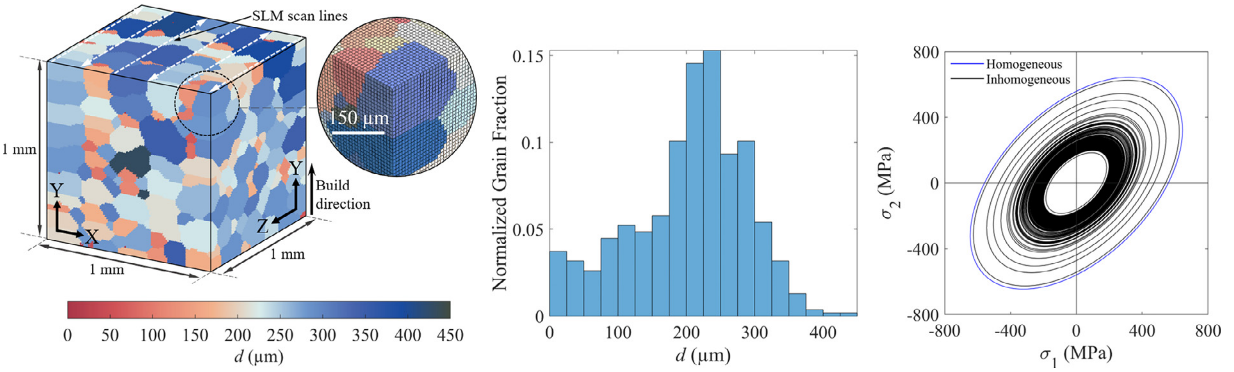

Fig. 4. (*Left*) Inhomogeneous microstructure predicted using the Dynamic KMC framework for SLM workpiece depicting the representative volume element (RVE) within the encircled region. (*Center*) Distribution of grains within the predicted inhomogeneous microstructure, per their respective major diameters, *d*. (*Right*) Maximum distortion-energy criterion yield surfaces for the SLM workpiece considering homogeneous and inhomogeneous microstructure modeling. (For interpretation of the reference to color in this figure, the reader is referred to the online version of this article.)

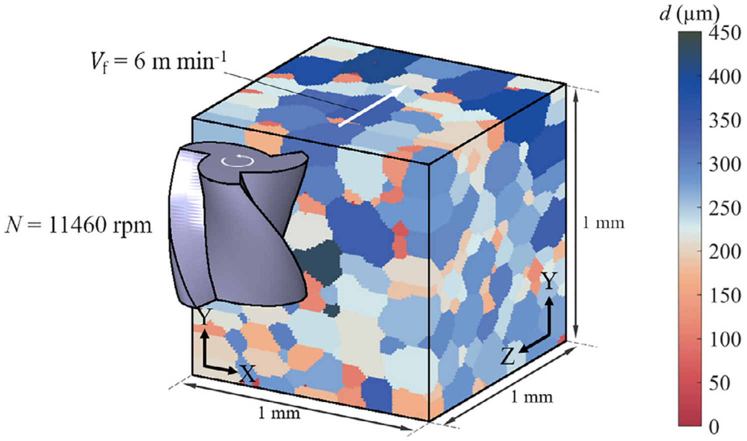

Fig. 5. Micro-milling simulation setup showing tool rotation and tool path relative to the SLM workpiece. (For interpretation of the reference to color in this figure, the reader is referred to the online version of this article.)

3. Case study 1: Micro-milling simulation

Fig. 5 illustrates the micro-milling simulation. Note that the diameter of the end milling tool (508 μm) is of the same order of magnitude as some of the larger grains (> 200 μm). This tool scale further elucidates the anisotropic response that results from modeling the microstructural inhomogeneity. While the nodal connectivity of the RVE Lagrangian FE model described in the previous section remains unchanged, coupled temperature-displacement elements with reduced integration are used to facilitate computation of RS and strain in the SLM cube workpiece during the micro-milling simulation. An element deletion technique is implemented for material removal, based on a linear-deformation failure criterion.

To capture the effects of strain rate and temperature dependency during plastic flow and material fracture, both a J-C constitutive (plasticity) model and a J-C damage initiation model, defined respectively by Eqs. (5) and (8), are applied (Johnson & Cook, 1983).

$$\sigma_f = \left[A + B(\varepsilon^{pl})^n\right]\left[1 + C\ \ln\left(\frac{\dot{\varepsilon}^{pl}}{\dot{\varepsilon}_0}\right)\right]\left[1 - (T^*)^m\right] \tag{5}$$

In Eq. (5), σ_f is the flow stress, A is the quasi-static yield stress that depends on H-P strengthening, B is the strain hardening coefficient, C is the strain-rate hardening coefficient, $\dot{\varepsilon}^{pl}$ is the plastic strain rate, $\dot{\varepsilon}_0$ is the reference strain rate, n is the strain hardening exponent, m is the thermal softening exponent, and T^* is a nondimensional temperature term given by Eq. (6).

$$T^* = \begin{cases} 0 & T < T_0 \\ \dfrac{T - T_0}{T_m - T_0} & T_0 \le T \le T_m \\ 1 & T > T_m \end{cases} \tag{6}$$

Table 6
Johnson–Cook parameters for inhomogeneous Inconel 625 used for the micro-milling simulation (Hokka et al., 2014; Lotfi, Jahanbakhsh, & Farid, 2016).

Johnson–Cook parameters	A (MPa)	B (MPa)	n	C	m	$\dot{\varepsilon}_0$ (s^{-1})	T_0 (K)	T_m (K)
Values	σ_y (based on Eq. (7))	2201.3	0.8	0.000209	1.146	1670	296	1623

Parameters for the J-C constitutive model determined via split Hopkinson pressure bar (SHPB) experiments (Hokka et al., 2014) are provided in Table 6. To capture the influence of grain size for the inhomogeneous case, or more specifically grain major diameter d_i, the J-C flow stress constitutive model is combined with the H-P relation given by Eq. (7), (Lindgren et al., 2016; Wang, Palmer, & Beese, 2016b).

$$\sigma_y = \sigma_0 + \frac{k_y}{\sqrt{d_i}} \tag{7}$$

In Eq. (7), σ_y is the quasi-static yield strength, σ_0 (105 MPa) is the minimum stress required to initiate dislocation movement, k_y (1380 MPa $\mu m^{0.5}$) is the strengthening coefficient for Inconel 625 (Gao & Zhou, 2018), and d_i is the individual grain's major diameter. It should be noted that the term d, although initially intended to be considered as the averaged grain diameter, has been reported to be used as individual grain diameter in recent studies (Lindgren et al., 2016). In effect, the modeling approach gives rise to numerous yield surfaces depicted by the black lines in Fig. 4 (*Right*). For the homogeneous case, σ_y is assumed to be 559 MPa (Hokka et al., 2014), representative of equiaxed grains of ~10 μm diameter as per Hall–Petch strengthening and is depicted by the single (blue) homogeneous yield surface seen in Fig. 4 (*Right*).

Fracture of the Inconel 625 alloy can be attributed to two mechanisms, namely ductile fracture and shear fracture. As described by Hooputra, Gese, Dell, & Werner (2004), based on phenomenological observations, damage criteria for both mechanisms need to be adopted. Accordingly, damage initiation criteria for fracture of metals that encompass ductile and shear behavior are applied for the milling simulation. Three independent damage initiation criteria are simultaneously implemented, including (1) the ductile criterion, (2) the Johnson–Cook criterion, and (3) the shear criterion. Each criterion is described by an output variable that is computed at every time increment for each element, defined on a scale of 0 to 1. A value of 1 indicates that the initiation criterion is met and the material stiffness for the element(s) can be degraded per a predefined damage evolution law for the specific criterion.

The onset of damage by nucleation, grain growth and coalescence of porosities is phenomenologically predicted by the ductile criterion, which assumes equivalent plastic strain at the onset of damage, γ_D, as a function of stress triaxiality, η, and plastic strain rate, $\dot{\varepsilon}^{pl}$. The damage criterion is met when Eq. (8) is satisfied. With the onset of plastic deformation, state variable (for ductile criterion), ω_D, increases monotonically. The incremental increase in ω_D with each time increment during the simulation is computed by Eq. (9).

$$\omega_D = \int \frac{d\varepsilon^{pl}}{\gamma_D(\eta, \dot{\varepsilon}^{pl})} = 1 \tag{8}$$

$$\Delta\omega_D = \frac{\Delta\varepsilon^{pl}}{\gamma_D(\eta, \dot{\varepsilon}^{pl})} \geq 0 \tag{9}$$

where,

$$\eta = -\frac{p}{q} \tag{10}$$

In Eq. (10) p is the pressure stress and q is the von Mises equivalent stress. The relationship between stress triaxiality and effective plastic strain to fracture adopted herein was reported by Matache, Paraschiv, & Condruz (2020), who performed tensile notch sensitivity experiments on Inconel 625 powder bed fusion cylindrical specimens.

Given that Eq. (8) does not capture the influence of temperature, in addition to the ductile damage criterion, the Johnson–Cook damage criterion presented in Eq. (11), is applied. This damage criterion is commonly implemented in conjunction with the Johnson–Cook plasticity definition for machining simulations (Ljustina et al., 2014; Pantalé, Bacaria, Dalverny, Rakotomalala, & Caperaa, 2004).

$$\gamma_D = [D_1 + D_2 e^{-D_3 \eta}]\left[1 + D_4 \ln\left(\frac{\dot{\varepsilon}^{pl}}{\dot{\varepsilon}_0}\right)\right][1 + D_5 T^*] \tag{11}$$

In Eq. (11), D_1 is the initial fracture strain, D_2 to D_5 represent the exponential, triaxiality, strain-rate and temperature parameters, respectively (Akram et al., 2018). The damage parameters used herein were experimentally determined by Erice & Gálvez (2014), and are listed in Table 7. Note that Eq. (11) differs from that originally published by Johnson & Cook (1985) with regard to the negative sign added to parameter D_3. This modification is driven by the decrease in γ_D, experienced by most materials, as η increases. While the J-C damage initiation model is not explicitly a function of the microstructure, it is indirectly dependent on microstructure through its dependency on milling-induced plastic strain, which

Table 7
Johnson–Cook damage initiation criterion parameters used for the micro-milling simulation (Erice & Gálvez, 2014; Xie, Yang, Ding, & Scarpa, 2019).

D_1	D_2	D_3	D_4	D_5
0.04	0.75	1.45	0.04	0.89

is governed by the J-C H-P flow stress modeling implemented by Eqs. (5)–(7). As mentioned above, for the inhomogeneous case, the flow stress of individual grains is influenced by their respective major diameters.

The onset of damage via shear band localization is phenomenologically predicted by the shear criterion, which assumes equivalent plastic strain at the onset of damage, γ_S, to be a function of shear stress ratio, τ_S, and plastic strain rate, $\dot{\varepsilon}^{pl}$. The damage criterion is met when Eq. (12) is satisfied. As per Eq. (12), with the onset of plastic deformation proportional to the incremental change in γ_S, the shear criterion state variable, ω_S, increases monotonically. The incremental increase in ω_S with each time increment during the simulation is computed via Eq. (13).

$$\omega_S = \int \frac{d\varepsilon^{pl}}{\gamma_S(\tau_S, \dot{\varepsilon}^{pl})} = 1 \tag{12}$$

$$\Delta\omega_S = \frac{\Delta\varepsilon^{pl}}{\gamma_S(\tau_S, \dot{\varepsilon}^{pl})} \geq 0 \tag{13}$$

where,

$$\tau_S = \frac{(1 + k_S p)}{\tau_{\max}} \tag{14}$$

In Eq. (14), $\tau_{\max}$ is the shear stress limit defined as $0.577\sigma_y$ per distortion-energy theory, and material parameter k_S is set as 1.57 as per (Zhu & Engelhardt, 2018).

Once one of the aforementioned damage initiation criteria is met, a damage evolution law given by Eq. (15) is required to describe the rate of degradation of the material stiffness. In Eq. (15), $\boldsymbol{\sigma}$ is the real-time stress tensor, D is the overall damage variable that captures a combined effect of all the active mechanisms, and $\boldsymbol{\sigma}^*$ is the undamaged stress tensor calculated for the given time increment. As D approaches a value of 1 the material loses its load-bearing capacity. When $D = 0.9$ at the integration point of an element, the corresponding element is deleted from the mesh, essential to the chip formation process.

$$\boldsymbol{\sigma} = (1 - \mathrm{D})\boldsymbol{\sigma}^* \tag{15}$$

Since multiple damage criteria are active, D is determined by whichever is the greatest at a given increment of time as described in Eq. (16), where $\mathrm{d_j}$ represents an individual damage variable corresponding to a given damage mechanism.

$$\mathrm{D} = \max(\mathrm{d_j}) \tag{16}$$

Once a damage initiation criterion is reached, the relationship of plastic distortion rate, $\dot{\mathrm{U}}^{pl}$, with the characteristic element length, L_e, rate of change of the given damage variable, $\dot{\mathrm{d}}_\mathrm{j}$, plastic strain rate, $\dot{\varepsilon}^{pl}$, and effective plastic distortion at the point of failure, U_f^{pl}, is defined using linear damage evolution law presented in Eq. (17).

$$\dot{\mathrm{d}} = \frac{L_e\dot{\varepsilon}^{pl}}{\mathrm{U}_f^{pl}} = \frac{\dot{\mathrm{U}}^{pl}}{\mathrm{U}_f^{pl}} \tag{17}$$

Per Eq. (17), the material stiffness is completely degraded, i.e., $d = 1$, once $\mathrm{U}^{pl} = \mathrm{U}_f^{pl}$. With the linear damage evolution law, provided the material response is perfectly plastic post damage initiation, a truly linear stress-strain softening response can be predicted.

3.1. Material and geometry of the micro-milling tool

A square-shouldered Sialon tool is modeled for the high-speed micro-milling of the SLM-fabricated Inconel cube workpiece (Schulz & Moriwaki, 1992). The ceramic tool is manufacturable such that its microstructure is ideal for high speed machining of superalloys and it performs well given the high temperatures (exceeding 1270 K) in the cutting zone. At such temperatures, thermal softening of the superalloy leads to a reduction in resisting forces acting on the cutting edge of the tool. The tool has been documented to successfully operate at high speed without fracturing or considerable micro-chipping, (Çelik, Alağaç, Turan, Kara, & Kara, 2017). To limit the computational cost, the deformable tool implemented in the FE model is discretized by linear hexahedral elements having an edge length of approximately 100 μm. While this may appear to be a relatively coarse mesh, it does not present a problem given that the stress developed in the tool is not studied in this

Table 8
Sialon material properties (Syalon).

Material Property	Values
Density	3240 kg m^{-3}
Young's modulus	288 GPa
Poisson's ratio	0.23
Thermal conductivity	28 W m^{-1} K^{-1}
Thermal expansion coefficient	3 × 10^{-6} K^{-1}
Specific heat	650 J kg^{-1} K^{-1}

Table 9
Micro-milling tool geometry and cutting parameters (Li et al., 2011b; Llanos et al., 2014 ; Tool Geometry).

Parameter	Values
Tool outer diameter	508 μm
Helix angle	30°
Number of flutes	3
Spindle speed, N	11460 rpm
Feed, f_N	0.52 mm rev^{-1}
Axial depth of cut	400 μm

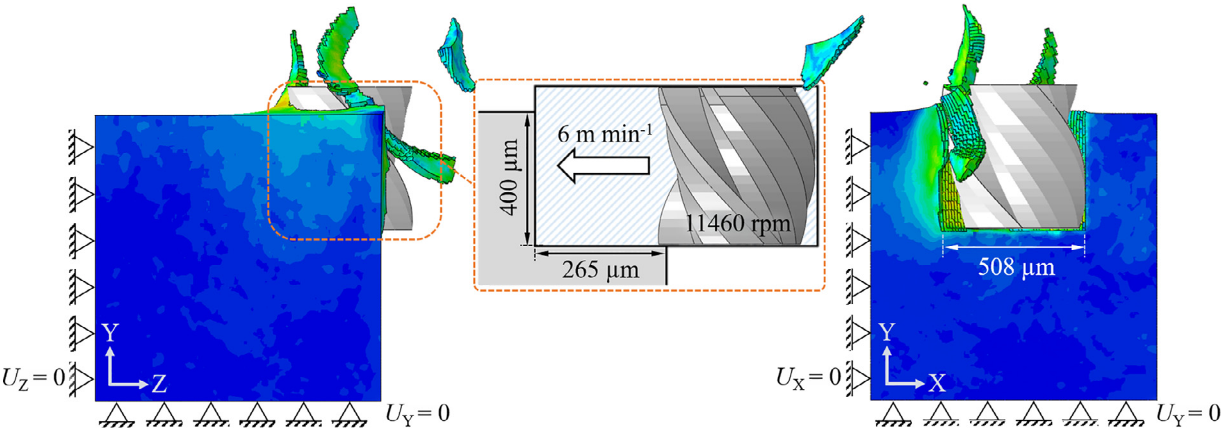

Fig. 6. Boundary conditions applied to the SLM workpiece during the micro-milling simulation.

work. Material properties for the Sialon tool are presented in Table 8 Syalon while tool geometry and cutting parameters are listed in Table 9 (Li, Oosterling, Hoogstrate, Langen, & Schmidt, 2011b; Llanos, Agirre, Urreta, Thepsonthi, & Özel, 2014), Tool Geometry.

3.2. Boundary conditions for the micro-milling simulation

As shown in Fig. 6, three orthogonal faces of the SLM cube workpiece have translational motion constrained. The displacement boundary conditions imposed are given by Eq. (18).

$$U_\beta = 0 \quad \text{on surface } \beta = 0 \quad \text{for } \beta = \{X, Y, Z\} \tag{18}$$

The tool has angular velocity, ω_Y, about its Y axis as well as a linear velocity, V_f, as specified by Eqs. (19) and (20), respectively.

$$\omega_Y = \frac{2\pi N}{60} \approx 1200 \text{ rad s}^{-1} \tag{19}$$

$$V_f = f_N N \approx 6 \text{ m min}^{-1} \quad (\text{in negative Z direction}) \tag{20}$$

Heat flux Q_f, generated via Coulomb friction, is described by Eq. (21), where Ψ is the plastic heat dissipation fraction (estimated at 0.9), μ is the friction coefficient, p_c is the tool-workpiece interface contact pressure, $\dot{s}$ is the slip rate (Renz, Khader, & Kailer, 2016).

$$Q_f = \Psi \mu p_c \dot{s} \tag{21}$$

Table 10
Parameters used to model the spatial and temporal distribution of the plasma pressure applied in the FE model (Fabbro, Fournier, Ballard, Devaux, & Virmont, 1990; Hatamleh, Mahadevan, Malik, Qian, & Kovacevic, 2019).

LSP parameters	Value
ND:YAG Laser pulse type	Q-switched
Laser beam wavelength	1064 nm
Full Width at Half Maximum (FWHM) pulse width, t_p	17 ns
Average pulse energy	2.5 J
Laser spot diameter	3.2 mm
Incident power density, I_0	3.11 GW cm^{-2}
Energy ratio, α	0.25
Adiabatic constant, λ	1.4
Absorbent coating	Polyvinyl chloride (PVC) black electrical insulation tape (Sundar et al., 2012)
Transparent overlay	Deionized water (approx. thickness: 0.85 to 0.95 mm)
Water shock impedance, Z_w	1.65×10^5 g cm^{-2} s^{-1}
Inconel 625 shock impedance, Z_{IN}	4.14×10^6 g cm^{-2} s^{-1} (Karthik, Stango, Vijayalakshmi, & Swaroop, 2017)
Gaussian spatial distribution standard deviation, σ_R	0.39 mm

Heat flux per unit volume Q_p, generated by mechanical dissipation associated with plastic strain rate of the workpiece material, is defined by Eq. (22).

$$Q_p = \Psi \boldsymbol{\sigma} : \dot{\varepsilon}^{pl} \tag{22}$$

Solutions for the micro-milling simulation are computed using the explicit solver of Abaqus v6.14, and are obtained at fixed time increments of 1.25 μs over the 6 ms process duration. A discussion on the results for the micro-milling simulation, with and without considering the inhomogeneous microstructure of the SLM fabricated workpiece, is given in Section 5, following a description of the modeling approach for the LSP post-process case study.

4. Case study 2: Laser shock peening simulation

In the laser shock peening (LSP) simulations, the effect of the laser fluence acting on the treated surface is captured by modeling the laser induced plasma pressure. The spatial and temporal distribution of the laser induced plasma pressure are based on corresponding experimental characterizations of the laser fluence, as discussed in the next section. The *single explicit analysis using time dependent damping* (SEATD) method, established by Hasser et al. to increase solution efficiency during LSP simulation, is implemented in this work (Hasser, Malik, Langer, Spradlin, & Hatamleh, 2016).

To ensure high fidelity of the temporal plasma pressure profile, solutions for the LSP shot are computed at time increments of 1 ns for the first 100 ns of its plasma-pressure history, during which plastic deformation is captured in the workpiece. This is followed by a 200 ns window of time-dependent damping that is applied to bring the model to a state of quasi-static equilibrium. As with micro-milling, the nodal connectivity of the RVE Lagrangian FE model for the SLM cube workpiece remains unchanged, however coupled temperature-displacement elements with reduced integration are assigned for the LSP post-process simulation.

The aforementioned J-C constitutive model integrated with the H-P strengthening as defined earlier in Eqs. (5)–(7), also applies for the LSP simulation. Thus, the same J-C material parameters specified earlier in Table 6 are used. Unlike the models presented by Wang et al. (2008) and Chen et al. (2007), strain rate dependency, hardening and dynamic loading effects are also captured by the demonstrated modeling framework. The damage initiation model incorporated for micro-milling is omitted, however, since fracture of the Inconel alloy at the tested LSP plasma pressure has not been observed experimentally (Rozmus-Górnikowska, Kusiński, & Cieniek, 2020).

4.1. Laser shock peening plasma pressure spatial and temporal profile

The spatial and temporal plasma pressure profiles used in this work are based on experimental characterization of the distribution and duration of the same pulsed laser beam reported by Hatamleh, Mahadevan, Malik, Qian, & Kovacevic, 2019. The laser source (*Spectra-Physics Quanta Ray Pro-350*) is a 3 J, Q-switched, 17 ns pulsed laser, operating at 1064 nm wavelength (i.e., near-infrared). Hatamleh et al. used a beam splitter to intercept optical signals that were further converted to electrical signals using a fast photodetector (*Ophir FPS-1*). The spatial field distribution was captured using a high-resolution camera (*Ophir SP928*) equipped with a charge coupled device (CCD) sensor, whilst a digital storage oscilloscope (*LeCroy Waverunner 204Xi*) was used concurrently to measure the electrical signal input and obtain a temporal profile for the laser pulse. Based on Hatamleh et al.'s experimental work, parameters considered when modeling the spatial and temporal distribution of pressure pulse in the FE model are summarized in Table 10.

The spatial distribution for the plasma pressure P is modeled with the portion of an axisymmetric Gaussian profile applied to the top surface (i.e., plane Z = 1 mm) of the SLM cube workpiece, as seen in Fig. 7 (*Left*). The normalized spatial pressure profile, $P(R)$, depicted in Fig. 7 (*Center*), is described by Eq. (23), where R is the radial distance from the center of

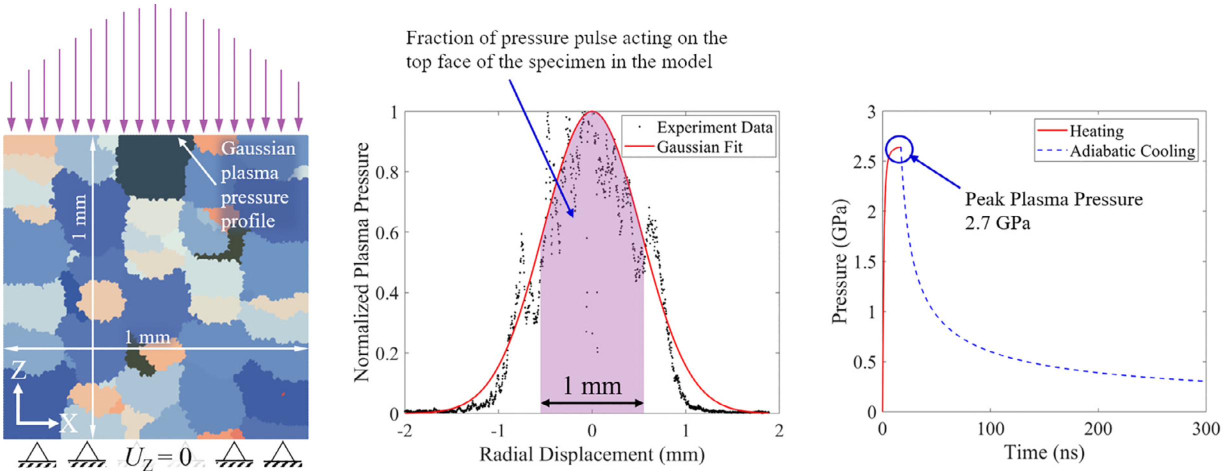

Fig. 7. (*Left*) Boundary conditions applied in the LSP simulation. (*Center*) Gaussian spatial distribution of the laser shot's plasma pressure. Shaded region represents the fraction of the plasma pressure acting directly on the surface (Z = 1 mm) of the SLM cube workpiece. (*Right*) Temporal profile of the plasma pressure used in the LSP post-process FE model.

the laser shot.

$$P(R) = \frac{1}{\sigma_R\sqrt{2\pi}} e^{\left[-\frac{1}{2}\left(\frac{R}{\sigma_R}\right)^2\right]}, \quad \text{for} \quad R \geq 0 \tag{23}$$

The peak plasma pressure (~2.7 GPa) and its temporal profile, $P(t)$, seen in Fig. 7 (*Right*), are computed using Fabbro et al.'s 1D hydrodynamic model (Fabbro, Fournier, Ballard, Devaux, & Virmont, 1990). They report that the temporal profile can be treated as a piecewise continuous function described by Eq. (24), representing both the heating phase ($0 < t < t_p$) and adiabatic cooling phase ($t \geq t_p$). In Eq. (24), L is the time-dependent plasma layer thickness, where the initial thickness, $L(0)$, is estimated as 300 μm.

$$P(t) = \begin{cases} \left\{\frac{1}{10}\left[\frac{\alpha Z I_0}{2\alpha+3}\right]\left[1-\left(\frac{L(0)}{L(t)}\right)^2\right]\right\}^{0.5}, & \text{for} \quad 0 < t < t_p \\ \mathrm{P}(t_p)\left[\frac{L(t_p)}{L(t)}\right]^{\lambda}, & \text{for} \quad t \geq t_p \end{cases} \tag{24}$$

where, the combined shock impedance (Z) can be calculated by Eq. (25).

$$Z = \frac{Z_{IN} Z_W}{2(Z_{IN} + Z_W)} \tag{25}$$

As illustrated in Fig. 7 (*Left*), nodes on bottom face of the SLM cube workpiece, i.e., surface coplanar with plane Z = 0 mm, are constrained with a zero vertical displacement (U_Z) boundary condition per Eq. (26), representative of conditions imposed by a rigid backplate upon which the workpiece would be secured during LSP treatment. Solutions for the LSP simulation are computed using the explicit solver of Abaqus v6.14.

$$U_Z = 0 \quad \text{on surface Z} = 0 \text{ mm} \tag{26}$$

5. Results and discussion on the influence of microstructure consideration on micro-milling and LSP simulations

5.1. Volumetric plastic strain and temperature distribution during the micro-milling simulation

To elucidate how the inclusion of microstructure modeling actively influences the real-time equivalent plastic strain, γ_{eq}, temperature, T, stress distribution, $\boldsymbol{\sigma}$, and damage initiation criteria, the discussion presented here examines a frame of time during the micro-milling operation at which the tool has progressed to a cut depth of approximately 265 μm (Z direction), as seen in Fig. 8 (*Top Left*). The region near the tool-workpiece interface where γ_{eq} is non-zero for a given frame of time, i.e. the "influence envelope", is illustrated in Fig. 8 (*Bottom Left*). The distribution of γ_{eq} and T around the tool during the micro-milling operation, when considering the inhomogeneous microstructure and when neglecting it, i.e., assuming homogeneity, are respectively illustrated in Fig. 8 (*Center*) and Fig. 8 (*Right*). Note, these are views of the upper surface of the workpiece with translucency enabled to offer a sense of the corresponding properties through its thickness (Y direction). Infrared thermography measurements collected by Saleem & Mumtaz (2020) during the face milling of Inconel 625 exhibited temperature variations in the range of 685 to 918 K, comparable to the temperature ranges predicted

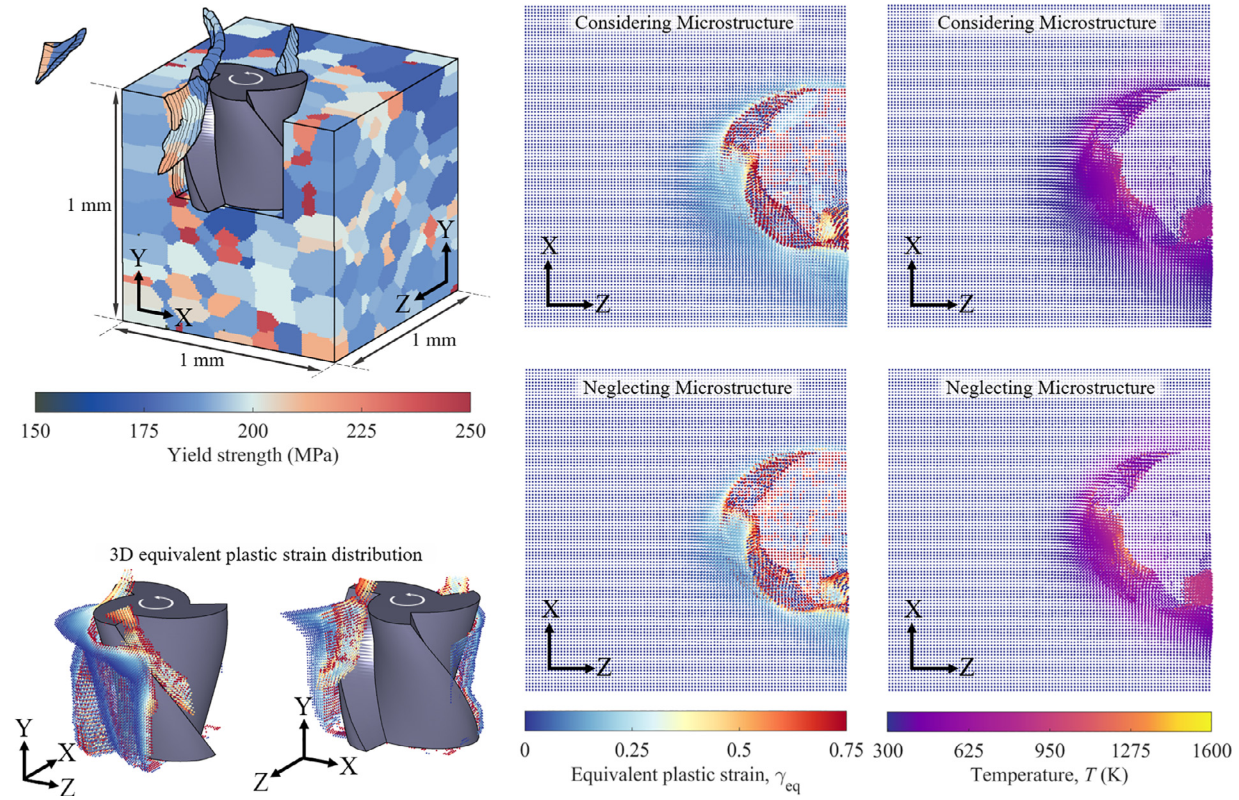

Fig. 8. (*Top Left*) Dimetric view during the micro-milling process showing microstructural inhomogeneity implemented by varying yield strength of individual grains per Hall–Petch strengthening (ref. Eq. (7)). (*Bottom Left*) Third-angle and first-angle dimetric views depicting 3D distribution of equivalent plastic strain around the tool in the inhomogeneous case. (*Center*) Effect of microstructure modeling on the equivalent plastic strain, γ_{eq}, during the micro-milling operation. (*Right*) Effect of microstructure modeling on the temperature distribution during the micro-milling operation. (For interpretation of the reference to color in this figure, the reader is referred to the online version of this article.)

herein. The coupled temperature-displacement model employs a Johnson–Cook (J-C) plasticity definition in conjunction with a J-C ductile damage initiation criterion, hence understanding the magnitude and distribution of γ_{eq} and T near the tool-workpiece interface is important. From Fig. 8 (*Center*) and Fig. 8 (*Right*) a clear difference in γ_{eq} and T is observed with the implementation of microstructural modeling; in the inhomogeneous case, the volumetric temperature distribution appears to be relatively greater, albeit for the homogeneous case, the peak temperature magnitude at the tool-workpiece interface is relatively higher. This can be expected, considering the differences of yield surfaces (ref. Fig. 4 (*Right*)) between the inhomogeneous and homogeneous models. Elongated (or columnar) grains in the inhomogeneous model, will plastically deform with much less resistance in comparison to the equivalent, smaller equiaxed grains in the homogeneous model considering Hall–Petch strengthening, when subject to the same amount to cutting and thrust force from the milling tool. In effect, the homogeneous model reveals a 27% greater contact pressure, p_c, and a 39% greater frictional shear stress in comparison to the inhomogeneous model. The resultant greater frictional heating, Q_f, in the homogeneous case explains the higher peak temperature predicted. In effect, higher shear stress and temperature magnitudes can be expected near the tool-workpiece interface in the homogeneous model, while a volumetrically larger distribution of plastic strain can be expected in the inhomogeneous model.

From Fig. 8 (*Top Left*), it is evident that dynamic recrystallization (DRX) phenomenon is not captured in the demonstrated modeling framework, however, its presence is implied by the predicted temperature and plastic strain distribution (Kruk et al., 2018). Inconel 625's stacking fault energy (215 mJ m^{-2}) (Nordström, Siriki, Moverare, & Chai, 2018) and the deformation temperature ($T < 1223$ K) predicted along the surface of the cut when considering microstructure (inhomogeneous case), suggests that dynamic recrystallization (DRX) phenomenon would be limited to material locations on/near the surface of the cut, and likely limited to small-scale, continuous DRX processes at the original grain boundaries, characterized by progressive subgrain rotation (Guo, Li, Guo, Peng, & Hu, 2011; Sakai, Belyakov, Kaibyshev, Miura, & Jonas, 2014). Given the range of deformation temperature, the size of the DRX grains will not increase with an increase in deformation strain (Li, Guo, Guo, Peng, & Wu, 2011a). Considering the face-centered cubic (FCC) crystal structure and stacking fault energy of Inconel 625, the common deformation mechanisms will be dislocation slip, during the initial stages of deformation, and twinning, as deformation progresses (Gao et al., 2019). Twinning due to intragranular shear deformation will impede dislocation motion and cause surface hardening (He, Chung, Lavernia, Liao, & Zhu, 2003). When neglecting microstructure (homogeneous case), deformation temperatures at the surface of the cut appear to exceed 1223 K, suggesting the onset of discontinuous DRX, with bulging grain boundaries and greater likelihood of twinning. At these higher deformation temperatures, DRX grains that stem from progressive subgrain rotation gradually move from the grain interior to the location of the original grain boundaries. As temperature increases beyond 1223 K, the DRX grain size and volume fraction will also increase. This demonstrates how microstructure modeling can influence the nature of DRX, as suggested by the variations of equivalent plastic strain and temperature.

5.2. Stress distribution and material removal during the micro-milling simulation

Inclusion of microstructure in the numerical model illuminates (1) variations in the real-time stress distribution and (2) a slight difference in the material removed, as seen in Fig. 9. Normal stress as well as in-plane and out-of-plane shear stress components are probed considering the different cutting force directions that arise from helical shape of the tool. Differences in stress patterns, particularly near the tool-workpiece interface, arise due to the variation in yield surfaces, as presented earlier in Fig. 4 (*Right*), when modeling microstructure using the J-C H-P approach. The "equivalent diameter" of equiaxed grains in the homogeneous case is approximately 10 μm, whereas in the inhomogeneous case, major diameters predicted by the Dynamic KMC method range from 10 μm (equiaxed grains) to 450 μm (columnar grains) as seen in Fig. 4 (*Center*). Accordingly, the homogeneous case implements a yield strength of 559 MPa, while the inhomogeneous case implements yield strengths ranging from 170 to 541 MPa. In effect, the flow stress of the homogeneous case is significantly greater in comparison to that demonstrated by the inhomogeneous case. Grain boundary sliding (GBS) effects can arise in the inhomogeneous case considering differences in flow stress between adjacent grains that may vary considerably in size. GBS influences the amount of intra- and intergranular distortion and equivalent plastic shear strain, γ_S, sustained before a chip breaks off during the milling simulation. When the strain rate, $\dot{\varepsilon}$, at a given location exceeds the alloy's reference GBS strain rate, $\dot{\varepsilon}_{GBS}$, the rate of boundary migration, diffusion flow and dislocation slip become insufficient and can no longer

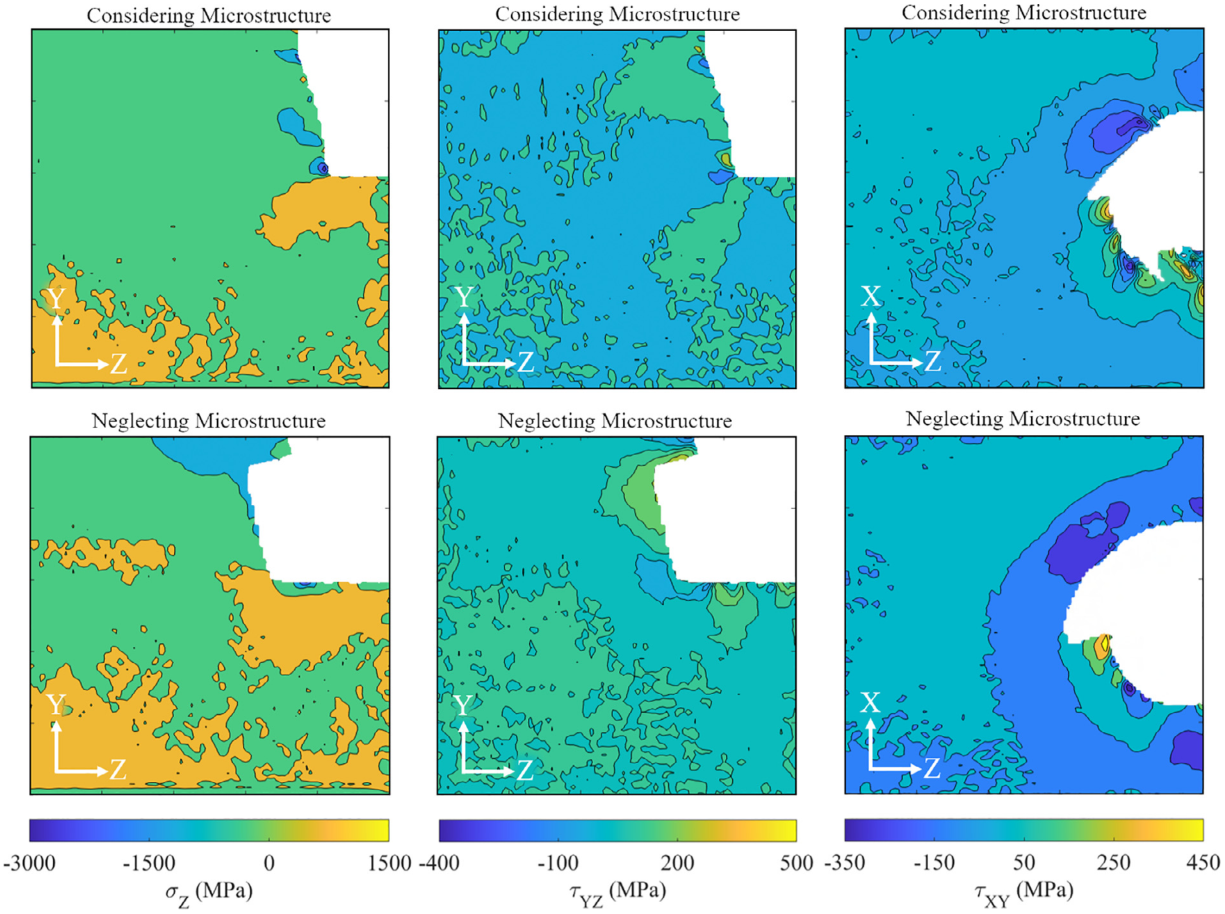

Fig. 9. (*Left to Right*) σ_Z and τ_{YZ}, on plane X = 0.5 mm, and τ_{XY} on plane Y = 0.9 mm when the tool has progressed to a cut depth of approximately 265 μm. (For interpretation of the reference to color in this figure, the reader is referred to the online version of this article.)

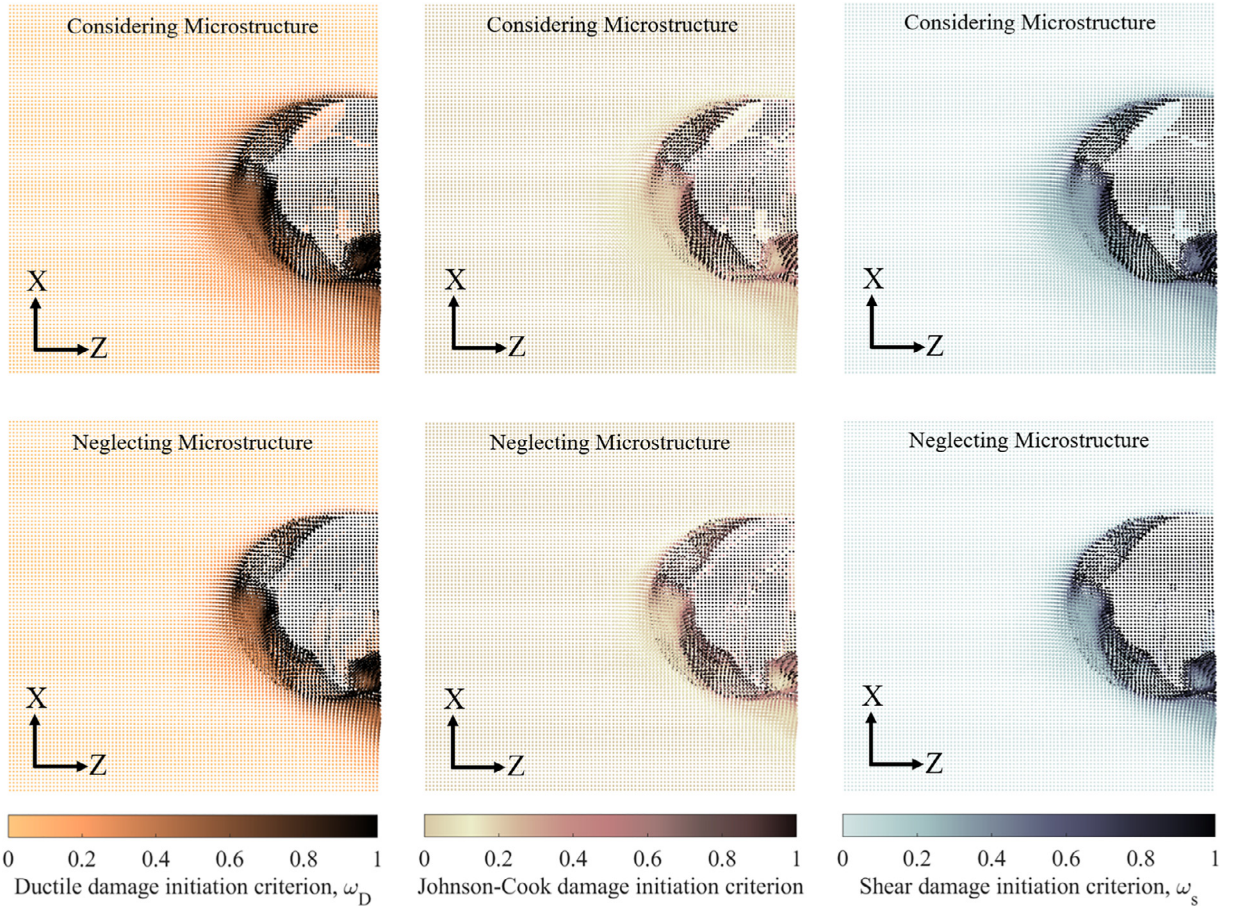

Fig. 10. Effect of microstructure modeling on the phenomenological damage initiation criteria. (*Left*) ductile damage, ω_D, (*Center*) Johnson–Cook damage, and (*Right*) shear damage, ω_S. (For interpretation of the reference to color in this figure, the reader is referred to the online version of this article.)

accommodate GBS. Localized compressive stresses appear at grain triple junctions, boundary ledges, and grain interiors, promoting intragranular plastic deformation and DRX (Liu & Nelson, 2018).

Stress contour plots captured at the same time increment during the respective simulations, as seen in Fig. 9, reveal ~6.15% net material removal (white regions in Fig. 9) when considering microstructure modeling, and ~6.22% when neglecting it. Given the identical boundary conditions implemented on the milling tool for both cases (ref. Fig. 6), the only plausible explanation for the difference in the material removed is the damage model criteria and consequent element deletion. Fig. 10 is presented to help visualize the magnitude of variation and progression in the damage criteria arising from the inhomogeneous and homogeneous modeling approaches at the given time increment. The damage criteria magnitudes reveal an analogous pattern to that observed for γ_{eq} and T. Statistically, the ductile damage criterion has 39.8% (inhomogeneous case) and 40.1% (homogeneous case) of elements within the influence envelope approaching a value of 1. In comparison, the J-C damage criterion has 33.7% (inhomogeneous case) and 31% (homogeneous case) of elements within the influence envelope approaching a value of 1, and the shear damage criterion has 26.3% (inhomogeneous case) and 28.8% (homogeneous case) of elements within the influence envelope approaching a value of 1. This difference is attributed to localized variation in stress triaxiality, η, that arises in the inhomogeneous case as a result of plastic strain localization (Collini, Moroni, & Pirondi, 2019; Sunny et al., 2021) in the RVE; inhomogeneity is introduced by modeling individual grains with unique yield surfaces based on their major diameter. This introduces the variations in η computed at different locations in the RVE for a given amount of hydrostatic stress applied. Varying the SLM parameters will result in a different RVE, with different yield surfaces, for grains at different locations. Accordingly, the computed η will also vary spatially, which can further influence the material removal, as well as the stress concentrations developed near the tool-workpiece interface. Thus, a process-structure-property relationship (Yan et al., 2018) is captured when microstructure modeling is implemented in the framework.

Anisotropic behavior of the material, although present in the inhomogeneous model, is not easily observed in the results of the micro-milling simulation, however, it is easily observable in the results of the LSP simulation, presented next.

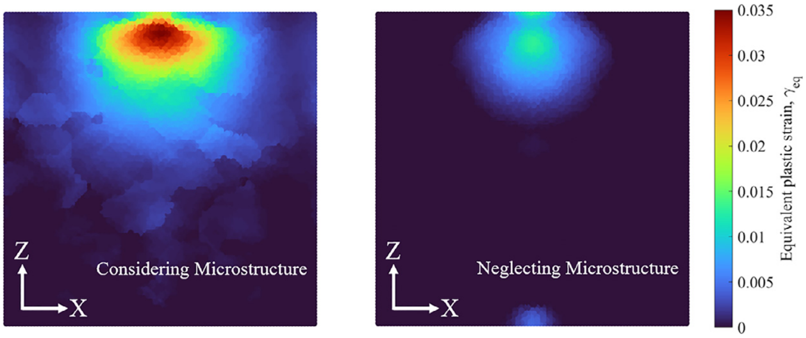

Fig. 11. Comparison of induced equivalent plastic strain, γ_{eq}, distribution in the workpiece after 1 LSP shot when considering (*Left*) and neglecting (*Right*) microstructure in the modeling approach. (For interpretation of the reference to color in this figure, the reader is referred to the online version of this article.)

5.3. Residual stress patterns predicted by laser shock peening simulations

Similar to the approach adopted for the milling simulations, LSP simulations are performed with and without implementing microstructure in the FE model, in order to elucidate how much of an influence (if any) it may have on the resulting RS distribution. As described earlier, a single LSP shot is applied to surface Z = 1 mm, while boundary conditions restrict vertical motion ($U_Z = 0$) at surface Z = 0 mm. While the peak equivalent plastic strain, γ_{eq}, induced by the LSP shot is very small in comparison to that seen with the micro-milling process, a very obvious difference arises with microstructure inclusion in the LSP FE model; Fig. 11 reveals an approximate 3-fold increase in peak γ_{eq} when microstructure is considered in the demonstrated work. The variation of yield surfaces, presented earlier in Fig. 4 (*Right*), explains the substantial difference predicted for the γ_{eq}. For the homogeneous model, which assumes equiaxed grains of approximately 10 μm diameter, yielding occurs only when the induced stress surpasses 559 MPa, whereas for the inhomogeneous case, where significantly larger grains that arise from the AM process (ref. Fig. 4 (*Center*)) are present, yielding can occur at sufficiently lower magnitudes of induced stress (~170 MPa) per Hall–Petch strengthening.

Fig. 12 demonstrates how anisotropy in the RS distribution is introduced by inclusion of microstructure in the FE model. Fig. 12 (*Left*) presents σ_X induced along the peened surface (Z = 1 mm), while Fig. 12 (*Center*) reveals σ_Y through the depth of the workpiece along cross sectional plane Y = 0.5 mm. While shear components are not typically examined in LSP experiments, to elucidate the influence of microstructure consideration on the LSP induced shear stress, the predicted in-plane component of shear stress, τ_{XY}, along the peened surface, is presented in Fig. 12 (*Right*). Comparing the predictions from the FE model, trends observed when considering and neglecting microstructure are summarized as follows:

1. RS distribution with perfect symmetry is predicted for normal stress components when neglecting microstructure, i.e., modeling the workpiece to be homogeneous. Similar results have been presented in the past by Warren et al. (Warren et al., 2008), Brockman et al. (2012), and Correa et al. (2015), whose work assumed isotropy and homogeneity in the specimen being treated. In the demonstrated work, these planes of symmetry include X = 0.5 mm and Y = 0.5 mm. When considering microstructure, i.e. modeling the workpiece as inhomogeneous, a trend that is somewhat symmetric about the same planes is exhibited, albeit perfect symmetry is not observed for normal stress components.
2. RS distribution with perfect symmetry is also predicted for shear stress components when neglecting microstructure, however, in comparison to that seen with normal stress components, the symmetry planes appear to rotate by an angle of 45°, i.e, planes Y = X and Y = 1 - X, in the demonstrated work. When considering microstructure, an asymmetric RS distribution is exhibited.
3. From Fig. 12, the magnitude of peak compressive and tensile RS induced via LSP treatment appears to be significantly greater when neglecting microstructure in the FE model. Some sparsely located localized peaks are exhibited when considering microstructure, however, the exact location of these peaks could vary with differences in mesh resolution. Rozmus-Górnikowska, Kusiński, & Cieniek, 2020, attributed the cracking of carbide precipitates on the LSP treated surface of their Inconel 625 specimen to large plastic deformation and/or high localized compressive RS induced via LSP, as is respectively exhibited from the inhomogeneous case of Figs. 11 and 12 (*Right*).

Comparing the difference in RS patterns of the homogeneous and inhomogeneous cases, Fig. 12 illuminates the importance of capturing anisotropy introduced in the numerical model by the inclusion of inhomogeneous microstructure arising from the AM process. Asymmetric RS patterns are predicted in the demonstrated work when considering microstructure, as was documented earlier by Chen et al. (2007) and Wang et al. (2008), despite differences the modeling approach. While the influence of crystal lattice orientation is not captured by the Dynamic KMC model, and hence neglected in the demonstrated work, the J-C H-P material definitions highlight the importance of having a grain size-dependent material constitutive model. Unrealistically symmetric patterns of RS and γ_{eq} that appear in the homogeneous case are eliminated by the anisotropic response predicted in the inhomogeneous case. In addition, changes in the SLM parameters, such as spot size, hatch spacing,

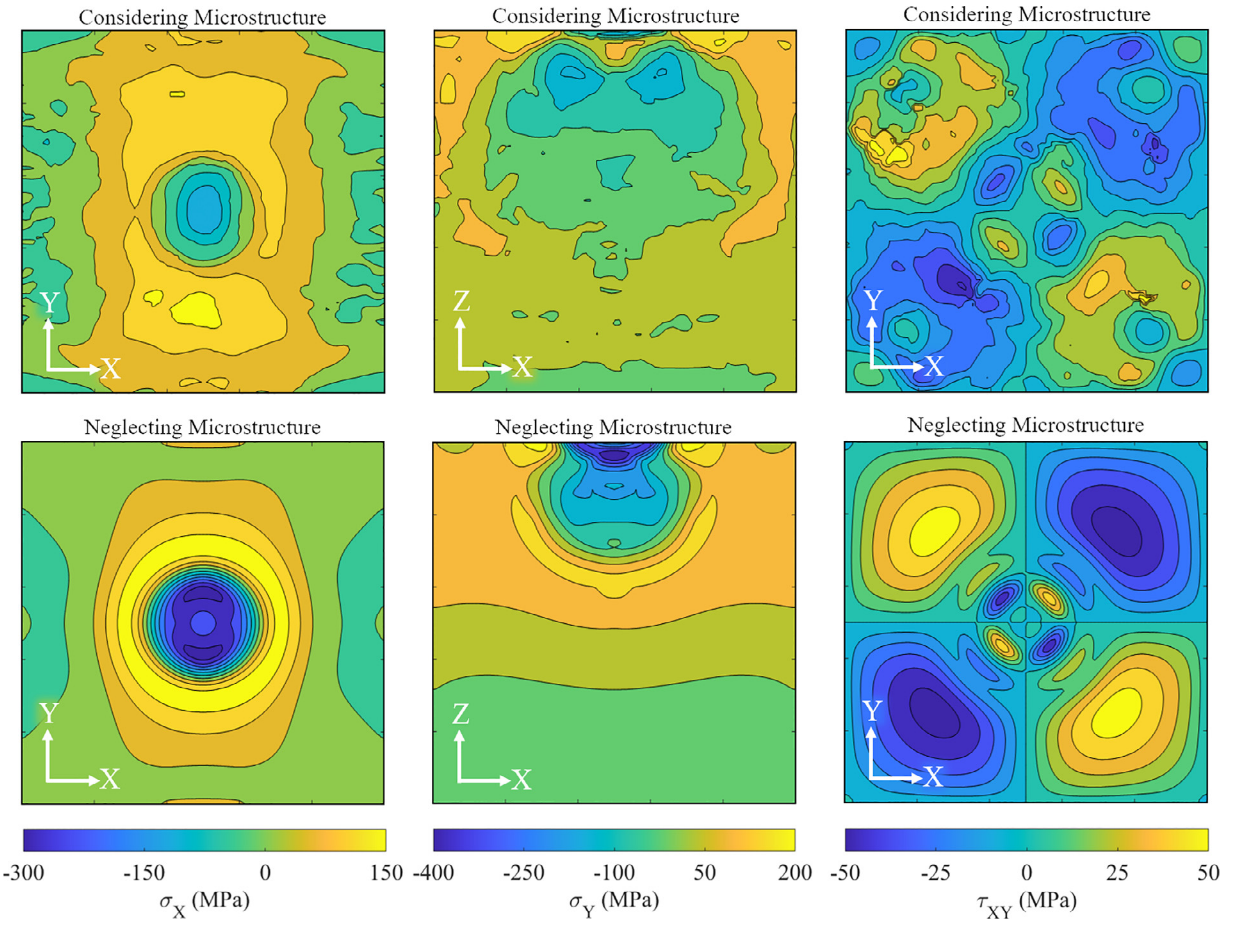

Fig. 12. (*Left*) σ_X on the top surface of the workpiece (Z = 1 mm). (*Center*) σ_Y viewed through the depth of the workpiece along cross sectional plane Y = 0.5 mm. (*Right*) τ_{XY} on the top surface of the workpiece (Z = 1 mm). (For interpretation of the reference to color in this figure, the reader is referred to the online version of this article.)

power and scan speed, can have a significant influence on the distribution of grains and grain morphology considering how these process parameters affect interlayer and intralayer heat accumulation during the AM build (Li & Soshi, 2019; Sunny, Yu, Mathews, Malik, & Li, 2021a). Hence, the process-structure-property relationship is captured.

A limitation of the existing work is that it does not capture the influence of AM residual stress on the post-process induced RS. The intent is to isolate and study post-process induced material response that stems from the microstructure modeling via Dynamic KMC. A recent study by Serrano-Munoz et al. (2021) illuminates the mutual dependence of AM residual stress and microstructure, hence in future work the AM process driven RS should also be considered. Moreover, this motivates further research opportunities, including examining the extent to which the AM RS influences the post-process induced residual stress, both with and without consideration of microstructure.

6. Conclusion

The demonstrated work elucidates the importance of considering microstructure in predictive models of machining operations and post-process treatments, especially when the microstructure is inhomogeneous as is the case with metal additive manufacturing. As discussed in the literature, existing measurement techniques such as X-ray diffraction have limited resolution and involve high levels of volumetric averaging, effectively masking the anisotropic response that arises given the microstructural inhomogeneity. While studies performed in the past relied on optical micrographs and EBSD images to develop 2D simulations which were limited to predicting in-plane response, the Dynamic Kinetic Monte Carlo algorithm is used herein to predict 3D microstructure for a given set of selective laser melting process parameters. The inhomogeneous microstructure RVE is then built into finite element models for micro-milling and laser shock peening operations, having considerably different strain rates. To illuminate the influence of microstructure on the results, identical cases for each simulation that neglect microstructure modeling are also executed. Key findings from both simulations, highlighting the importance of microstructure modeling are summarized as follows:

Micro-milling simulation:

- Greater frictional heating, Q_f, in the homogeneous case, stems from the relatively greater contact pressure and frictional shear stress, resulting in higher peak temperatures predicted at the tool-workpiece interface, albeit the volumetric temperature distribution for the inhomogeneous case appears to be relatively larger.
- Higher shear stress and temperature magnitudes are predicted near the tool-workpiece interface in the homogeneous model, while a volumetrically larger distribution of plastic strain is predicted in the inhomogeneous model.
- The presence of dynamic recrystallization is implied by the predicted temperature and plastic strain distribution.
- Differences in stress patterns, particularly near the tool-workpiece interface, arise due to the variation in yield surfaces in the inhomogeneous case, per Hall–Petch strengthening. Grain boundary sliding can arise from variations in flow stress of adjacent grains, influencing the amount of intra- and intergranular distortion and equivalent plastic shear strain, sustained before chip formation.
- Varying the SLM parameters will result in a different RVE, with different in yield surfaces, for grains at different locations. Accordingly, the computed stress triaxiality will vary spatially, which influences the material removal, as well as the stress concentrations developed near the tool-workpiece interface. Thus, a process-structure-property relationship is captured when considering microstructure in the model.

Laser shock peening simulation:

- Considering the variation in grain major diameter between the inhomogeneous case (10 to 450 μm) and the equivalent homogeneous case (10 μm), the equivalent plastic strain predicted for the inhomogeneous case was found to be three times higher in the demonstrated work, given the variation of yield surfaces as per Hall–Petch strengthening.
- Magnitudes of peak compressive and tensile residual stress induced via LSP are found to be significantly greater in the homogeneous model considering the higher flow stress in comparison to that for the inhomogeneous model. Localized peaks predicted for the LSP induced residual stress of the inhomogeneous case are much lower in magnitude to those of the homogeneous case.
- Asymmetric residual stress distributions are revealed when considering microstructural inhomogeneity, however, an unrealistically symmetric RS distribution is predicted with the homogeneous model, illuminating the importance of capturing anisotropy introduced in the numerical model via inclusion of microstructure modeling.

Declaration of Competing Interest

The authors declare that they have no known competing financial interests or personal relationships that could have appeared to influence the work reported in this paper.

Acknowledgments

Authors acknowledge the support of NSF CMMI-1762722. Any opinions, findings, or conclusions expressed in this paper are those of the authors and do not necessarily reflect the views of the National Science Foundation.

References

Akram, S., Jaffery, S. H. I., Khan, M., Fahad, M., Mubashar, A., & Ali, L. (2018). Numerical and experimental investigation of Johnson–Cook material models for aluminum (Al 6061-T6) alloy using orthogonal machining approach. *Advances in Mechanical Engineering, 10*(9). 1687814018797794.

Antonysamy, A. A., Meyer, J., & Prangnell, P. (2013). Effect of build geometry on the β-grain structure and texture in additive manufacture of Ti-6Al-4V by selective electron beam melting. *Materials Characterization, 84*, 153–168.

Bammann, D., Chiesa, M., Johnson, G., et al. (1996). Modeling large deformation and failure in manufacturing processes. *Theoretical and Applied Mechanics, 9*, 359–376.

Brockman, R. A., Braisted, W. R., Olson, S. E., Tenaglia, R. D., Clauer, A. H., Langer, K., & Shepard, M. J. (2012). Prediction and characterization of residual stresses from laser shock peening. *International journal of fatigue, 36*(1), 96–108.

Carlsson, K. (2013). *Modeling of three dimensional microstructures including grain boundary mechanisms*. Gothenburg, Sweden: Chalmers University of Technology.

Çelik, A., Alağaç, M. S., Turan, S., Kara, A., & Kara, F. (2017). Wear behavior of solid SiALON milling tools during high speed milling of Inconel 718. *Wear, 378*, 58–67.

Chen, H., Wang, Y., Kysar, J. W., & Yao, Y. L. (2007). Study of anisotropic character induced by microscale laser shock peening on a single crystal aluminum. *Journal of Applied Physics, 101*(2), 024904.

Chen, L., Sun, Y., Li, L., & Ren, X. (2020a). Microstructural evolution and mechanical properties of selective laser melted a nickel-based superalloy after post treatment. *Materials Science and Engineering: A, 792*, 139649.

Chen, Q., Zhao, Y., Strayer, S., Zhao, Y., Aoyagi, K., Koizumi, Y., … To, A. C. (2020b). Elucidating the effect of preheating temperature on melt pool morphology variation in Inconel 718 laser powder bed fusion via simulation and experiment. *Additive Manufacturing, 37*, 101642.

Chuzhoy, L., DeVor, R., Kapoor, S. G., & Bammann, D. (2002). Microstructure-level modeling of ductile iron machining. *Journal of Manufacturing Science and Engineering, 124*(2), 162–169.

Collini, L., Moroni, F., & Pirondi, A. (2019). Modeling the influence of stress triaxiality on the failure strain of nodular cast iron microstructures. *Procedia Structural Integrity, 18*, 671–687.

Correa, C., Peral, D., Porro, J., Díaz, M., de Lara, L. R., García-Beltrán, A., & Ocaña, J. (2015). Random-type scanning patterns in laser shock peening without absorbing coating in 2024-t351 al alloy: A solution to reduce residual stress anisotropy. *Optics & Laser Technology, 73*, 179–187.

Cuellar, S. D., Hill, M. R., DeWald, A. T., & Rankin, J. E. (2012). Residual stress and fatigue life in laser shock peened open hole samples. *International Journal of Fatigue, 44*, 8–13.

Daw, J., Rempe, J., & Knudson, D. (2010). Thermal properties of structural materials used in LWR vessels. *Journal of Nuclear Materials, 401*(1–3), 65–70.

Denlinger, E. R., Gouge, M., Irwin, J., & Michaleris, P. (2017). Thermomechanical model development and in-situ experimental validation of the laser powder-bed fusion process. *Additive Manufacturing, 16*, 73–80.

Denlinger, E. R., & Michaleris, P. (2016). Effect of stress relaxation on distortion in additive manufacturing process modeling. *Additive Manufacturing, 12*, 51–59.

Erice, B., & Gálvez, F. (2014). A coupled elastoplastic-damage constitutive model with lode angle dependent failure criterion. *International Journal of Solids and Structures, 51*(1), 93–110.

Fabbro, R., Fournier, J., Ballard, P., Devaux, D., & Virmont, J. (1990). Physical study of laser-produced plasma in confined geometry. *Journal of Applied Physics, 68*(2), 775–784.

Gao, Y., Ding, Y., Chen, J., Xu, J., Ma, Y., & Wang, X. (2019). Effect of twin boundaries on the microstructure and mechanical properties of Inconel 625 alloy. *Materials Science and Engineering: A, 767*, 138361.

Gao, Y., & Zhou, M. (2018). Superior mechanical behavior and fretting wear resistance of 3D-printed Inconel 625 superalloy. *Applied Sciences, 8*(12), 2439.

Goldak, J., Chakravarti, A., & Bibby, M. (1984). A new finite element model for welding heat sources. *Metallurgical Transactions B, 15*(2), 299–305.

Gouge, M., & Michaleris, P. (2017). *Thermomechanical modeling of additive manufacturing*. Butterworth-Heinemann.

Guo, Q., Li, D., Guo, S., Peng, H., & Hu, J. (2011). The effect of deformation temperature on the microstructure evolution of Inconel 625 superalloy. *Journal of Nuclear Materials, 414*(3), 440–450.

Hahn, D. W., & Özisik, M. N. (2012). *Heat conduction*. John Wiley & Sons.

Hasser, P. J., Malik, A. S., Langer, K., Spradlin, T. J., & Hatamleh, M. I. (2016). An efficient reliability-based simulation method for optimum laser peening treatment. *Journal of Manufacturing Science and Engineering, 138*(11), 111001–1–111001–14.

Hatamleh, M. I., Mahadevan, J., Malik, A., Qian, D., & Kovacevic, R. (2019). Prediction of residual stress random fields for selective laser melted A357 aluminum alloy subjected to laser shock peening. *Journal of Manufacturing Science and Engineering, 141*(10), 101011–1–101011–14.

He, J., Chung, K. H., Lavernia, E. J., Liao, X., & Zhu, Y. T. (2003). Mechanical milling-induced deformation twinning in Fcc materials with high stacking fault energy. *Metallurgical and Materials Transactions A, 34*(3), 707–712.

Heigel, J., Michaleris, P., & Reutzel, E. W. (2015). Thermo-mechanical model development and validation of directed energy deposition additive manufacturing of Ti-6Al-4V. *Additive Manufacturing, 5*, 9–19.

Heigel, J. C., & Lane, B. M. (2018). Measurement of the melt pool length during single scan tracks in a commercial laser powder bed fusion process. *Journal of Manufacturing Science and Engineering, 140*(5), 051012-1–051012-7.

Hokka, M., Gomon, D., Shrot, A., Leemet, T., Bäker, M., & Kuokkala, V.-T. (2014). Dynamic behavior and high speed machining of Ti-6246 and alloy 625 superalloys: Experimental and modeling approaches. *Experimental Mechanics, 54*(2), 199–210.

Hooputra, H., Gese, H., Dell, H., & Werner, H. (2004). A comprehensive failure model for crashworthiness simulation of aluminium extrusions. *International Journal of Crashworthiness, 9*(5), 449–464.

Johnson, G. R., & Cook, W. H. (1983). A constitutive model and data for metals subjected to large strains, high strain rates and high temperatures. In *Proceedings of the 7th international symposium on ballistics, The Netherlands: vol. 21* (pp. 541–547).

Johnson, G. R., & Cook, W. H. (1985). Fracture characteristics of three metals subjected to various strains, strain rates, temperatures and pressures. *Engineering Fracture Mechanics, 21*(1), 31–48.

Johnson, K. L., Rodgers, T. M., Underwood, O. D., Madison, J. D., Ford, K. R., Whetten, S. R., … Bishop, J. E. (2018). Simulation and experimental comparison of the thermo-mechanical history and 3D microstructure evolution of 304l stainless steel tubes manufactured using lens. *Computational Mechanics, 61*(5), 559–574.

Karthik, D., Stango, S. A. X., Vijayalakshmi, U., & Swaroop, S. (2017). Electrochemical behavior of laser shock peened inconel 625 superalloy. *Surface and Coatings Technology, 311*, 46–54.

Kruk, A., Wusatowska-Sarnek, A., Ziętara, M., Jemielniak, K., Siemiątkowski, Z., & Czyrska-Filemonowicz, A. (2018). Characterization on white etching layer formed during ceramic milling of Inconel 718. *Metals and Materials International, 24*(5), 1036–1045.

de La Batut, B., Fergani, O., Brotan, V., Bambach, M., & El Mansouri, M. (2017). Analytical and numerical temperature prediction in direct metal deposition of Ti-6Al-4V. *Journal of Manufacturing and Materials Processing, 1*(1), 3.

Lane, B., Moylan, S., Whitenton, E. P., & Ma, L. (2016). Thermographic measurements of the commercial laser powder bed fusion process at NIST. *Rapid prototyping journal*.

Li, D., Guo, Q., Guo, S., Peng, H., & Wu, Z. (2011a). The microstructure evolution and nucleation mechanisms of dynamic recrystallization in hot-deformed Inconel 625 superalloy. *Materials and Design, 32*(2), 696–705.

Li, P., Oosterling, J., Hoogstrate, A., Langen, H., & Schmidt, R. M. (2011b). Design of micro square end-mills for hard milling applications. *The International Journal of Advanced Manufacturing Technology, 57*(9–12), 859–870.

Li, W., & Soshi, M. (2019). Modeling analysis of the effect of laser transverse speed on grain morphology during directed energy deposition process. *The International Journal of Advanced Manufacturing Technology, 103*(9–12), 3279–3291.

Lindgren, L.-E., Lundbäck, A., Fisk, M., Pederson, R., & Andersson, J. (2016). Simulation of additive manufacturing using coupled constitutive and microstructure models. *Additive Manufacturing, 12*, 144–158.

Liu, F., & Nelson, T. (2018). Grain structure evolution, grain boundary sliding and material flow resistance in friction welding of alloy 718. *Materials Science and Engineering: A, 710*, 280–288.

Ljustina, G., Larsson, R., & Fagerström, M. (2014). A Fe based machining simulation methodology accounting for cast iron microstructure. *Finite Elements in Analysis and Design, 80*, 1–10.

Llanos, I., Agirre, A., Urreta, H., Thepsonthi, T., & Özel, T. (2014). Micromilling high aspect ratio features using tungsten carbide tools. *Proceedings of the Institution of Mechanical Engineers, Part B: Journal of Engineering Manufacture, 228*(11), 1350–1358.

Lotfi, M., Jahanbakhsh, M., & Farid, A. A. (2016). Wear estimation of ceramic and coated carbide tools in turning of Inconel 625: 3D Fe analysis. *Tribology International, 99*, 107–116.

Lu, Y., Pan, Z., Bocchini, P., Garmestani, H., & Liang, S. (2019). Grain size sensitive-MTS model for Ti-6Al-4V machining force and residual stress prediction. *The International Journal of Advanced Manufacturing Technology, 102*(5–8), 2173–2181.

MacDougall, D., & Maudlin, P. (2000). The Proportion of Plastic Work Converted to Heat in Ti-6Al-4V: MTS Model Prediction and Experimental Data. *Technical Report*. Los Alamos National Lab., NM (US).

Madireddy, G., Li, C., Liu, J., & Sealy, M. P. (2019). Modeling thermal and mechanical cancellation of residual stress from hybrid additive manufacturing by laser peening. *Nanotechnology and Precision Engineering, 2*(2), 49–60.

Manvatkar, V., Gokhale, A., Reddy, G. J., Venkataramana, A., & De, A. (2011). Estimation of melt pool dimensions, thermal cycle, and hardness distribution in the laser-engineered net shaping process of austenitic stainless steel. *Metallurgical and materials transactions A, 42*(13), 4080–4087.

Matache, G., Paraschiv, A., & Condruz, M. R. (2020). Tensile notch sensitivity of additively manufactured in 625 superalloy. *Materials, 13*(21), 4859.

Michaleris, P. (2014). Modeling metal deposition in heat transfer analyses of additive manufacturing processes. *Finite Elements in Analysis and Design, 86*, 51–60.

Moylan, S., Whitenton, E., Lane, B., & Slotwinski, J. (2014). Infrared thermography for laser-based powder bed fusion additive manufacturing processes. In *Aip conference proceedings: vol. 1581* (pp. 1191–1196). American Institute of Physics.

Nordström, J., Siriki, R., Moverare, J., & Chai, G. (2018). Deformation twinning behavior in high Ni-austenitic materials. In *Materials science forum: vol. 941* (pp. 1591–1596). Trans Tech Publ.

Pan, Z., Feng, Y., Ji, X., & Liang, S. Y. (2018). Turning induced residual stress prediction of AISI 4130 considering dynamic recrystallization. *Machining Science and Technology, 22*(3), 507–521.

Pan, Z., Liang, S. Y., & Garmestani, H. (2019a). Finite element simulation of residual stress in machining of Ti-6Al-4V with a microstructural consideration. *Proceedings of the Institution of Mechanical Engineers, Part B: Journal of Engineering Manufacture, 233*(4), 1103–1111.

Pan, Z., Shih, D. S., Garmestani, H., & Liang, S. Y. (2019b). Residual stress prediction for turning of Ti-6Al-4V considering the microstructure evolution. *Proceedings of the Institution of Mechanical Engineers, Part B: Journal of Engineering Manufacture, 233*(1), 109–117.

Pantalé, O., Bacaria, J.-L., Dalverny, O., Rakotomalala, R., & Caperaa, S. (2004). 2D and 3D numerical models of metal cutting with damage effects. *Computer Methods in Applied Mechanics and Engineering, 193*(39–41), 4383–4399.

Parida, A. K., & Maity, K. (2018). Comparison the machinability of Inconel 718, Inconel 625 and Monel 400 in hot turning operation. *Engineering Science and Technology, an International Journal, 21*(3), 364–370.

Ratchev, S., Afazov, S., Becker, A., & Liu, S. (2011). Mathematical modelling and integration of micro-scale residual stresses into axisymmetric Fe models of Ti6Al4V alloy in turning. *CIRP Journal of Manufacturing Science and Technology, 4*(1), 80–89.

Renz, A., Khader, I., & Kailer, A. (2016). Tribochemical wear of cutting-tool ceramics in sliding contact against a nickel-base alloy. *Journal of the European Ceramic Society, 36*(3), 705–717.

Rodgers, T., Bishop, J. E., & Madison, J. D. (2018). Direct Numerical Simulation of Mechanical Response in Synthetic Additive Manufacturing Microstructures.. *Technical Report*. Sandia National Lab.(SNL-NM), Albuquerque, NM (United States).

Rozmus-Górnikowska, M., Kusiński, J., & Cieniek, Ł. (2020). Effect of laser shock peening on the microstructure and properties of the Inconel 625 surface layer. *Journal of Materials Engineering and Performance, 29(3)*, 1544–1549.

Sakai, T., Belyakov, A., Kaibyshev, R., Miura, H., & Jonas, J. J. (2014). Dynamic and post-dynamic recrystallization under hot, cold and severe plastic deformation conditions. *Progress in Materials Science, 60*, 130–207.

Saleem, M. Q., & Mumtaz, S. (2020). Face milling of Inconel 625 via wiper inserts: Evaluation of tool life and workpiece surface integrity. *Journal of Manufacturing Processes, 56*, 322–336.

Schajer, G. S. (2013). *Practical residual stress measurement methods*. John Wiley & Sons.

Schulz, H., & Moriwaki, T. (1992). High-speed machining. *CIRP Annals, 41*(2), 637–643.

Serrano-Munoz, I., Fritsch, T., Mishurova, T., Trofimov, A., Apel, D., Ulbricht, A., … Bruno, G. (2021). On the interplay of microstructure and residual stress in LPBF IN718. *Journal of Materials Science, 56*(9), 5845–5867.

Shrestha, S., Starr, T., & Chou, K. (2018). Porosity analysis in metal additive manufacturing by micro-ct. *Asme international mechanical engineering congress and exposition*: vol. 52019. American Society of Mechanical Engineers. V002T02A059

Shrestha, S., Starr, T., & Chou, K. (2019). A study of keyhole porosity in selective laser melting: Single-track scanning with micro-ct analysis. *Journal of Manufacturing Science and Engineering, 141*(7), 071004-1–071004-11.

Sundar, R., Kumar, H., Kaul, R., Ranganathan, K., Tiwari, P., Kukreja, L., & Oak, S. (2012). Studies on laser peening using different sacrificial coatings. *Surface Engineering, 28*(8), 564–568.

Sunny, S., Gleason, G., Mathews, R., & Malik, A. (2021). Simulation of laser impact welding for dissimilar additively manufactured foils considering influence of inhomogeneous microstructure. *Materials and Design, 198*, 109372.

Syalon 101, physical property data for syalon 101. https://www.syalons.com/materials/silicon-nitride-sialon/syalon-101/. Accessed: 2020-11-22.

Tool Geometry, micro-milling tool geometry 5572375. https://www.kodiakcuttingtools.com/viewproducts/carbide-end-mills-3-flute-micro-long-reach-stub-flute-end-mills-altin-coated. Accessed: 2020-11-22.

Sunny, S., Yu, H., Mathews, R., Malik, A., & Li, W. (2021a). Improved grain structure prediction in metal additive manufacturing using a dynamic kinetic monte carlo framework. *Additive Manufacturing, 37*, 101649.

Trosch, T., Strößner, J., Völkl, R., & Glatzel, U. (2016). Microstructure and mechanical properties of selective laser melted Inconel 718 compared to forging and casting. *Materials Letters, 164*, 428–431.

Wang, P., Zhang, B., Tan, C. C., Raghavan, S., Lim, Y.-F., Sun, C.-N., … Chi, D. (2016a). Microstructural characteristics and mechanical properties of carbon nanotube reinforced Inconel 625 parts fabricated by selective laser melting. *Materials and Design, 112*, 290–299.

Wang, Y., Kysar, J. W., & Yao, Y. L. (2008). Analytical solution of anisotropic plastic deformation induced by micro-scale laser shock peening. *Mechanics of Materials, 40*(3), 100–114.

Wang, Z., Denlinger, E., Michaleris, P., Stoica, A. D., Ma, D., & Beese, A. M. (2017). Residual stress mapping in Inconel 625 fabricated through additive manufacturing: Method for neutron diffraction measurements to validate thermomechanical model predictions. *Materials and Design, 113*, 169–177.

Wang, Z., Palmer, T. A., & Beese, A. M. (2016b). Effect of processing parameters on microstructure and tensile properties of austenitic stainless steel 304l made by directed energy deposition additive manufacturing. *Acta Materialia, 110*, 226–235.

Warren, A., Guo, Y., & Chen, S. (2008). Massive parallel laser shock peening: Simulation, analysis, and validation. *International Journal of Fatigue, 30*(1), 188–197.

Wu, H., & Zhang, S. (2014). 3D FEM simulation of milling process for titanium alloy Ti-6Al-4V. *The International Journal of Advanced Manufacturing Technology, 71*(5–8), 1319–1326.

Xie, W., Yang, F., Ding, L., & Scarpa, F. (2019). Predictive models and experiments for high-velocity and high-temperature impacts in Inconel-alloy panels. *Materials and Design, 182*, 108032.

Yan, W., Lin, S., Kafka, O. L., Yu, C., Liu, Z., Lian, Y., … Liu, W. K. (2018). Modeling process-structure-property relationships for additive manufacturing. *Frontiers of Mechanical Engineering, 13*(4), 482–492.

Zhao, X., Iyer, A., Promoppatum, P., & Yao, S.-C. (2017). Numerical modeling of the thermal behavior and residual stress in the direct metal laser sintering process of titanium alloy products. *Additive Manufacturing, 14*, 126–136.

Zhong, C., Kittel, J., Gasser, A., & Schleifenbaum, J. H. (2019). Study of nickel-based super-alloys Inconel 718 and Inconel 625 in high-deposition-rate laser metal deposition. *Optics and Laser Technology, 109*, 352–360.

Zhou, L., Li, Y., He, W., He, G., Nie, X., Chen, D., … An, Z. (2013). Deforming TC6 titanium alloys at ultrahigh strain rates during multiple laser shock peening. *Materials Science and Engineering: A, 578*, 181–186.

Zhu, Y., & Engelhardt, M. D. (2018). Prediction of ductile fracture for metal alloys using a shear modified void growth model. *Engineering Fracture Mechanics, 190*, 491–513.